Laser-based Additive Manufacturing
Department of Mechanical Engineering
Technical University of Munich

Investigation of multispectral imaging algorithm for temperature determination on a numerical experiment platform in Laser-based Powder Bed Fusion of Metals

Untersuchung des multispektralen Bildgebungsverfahrens zur Temperaturbestimmung auf einer numerischen Experimentierplattform beim Laserbasierten Pulverbett-Schmelzverfahren von Metallen.

Semester Thesis

at the Department of Mechanical Engineering of the Technical University of Munich

Supervised by Prof. Dr.-Ing. Katrin Wudy
M.Sc. Ruihang Dai
Laser-based Additive Manufacturing

Submitted by Zhaoyong Wang
Connollystr.3
80809 München

Submitted on August 29, 2023 in Garching

Scope of Work

Title of the Semester Thesis:
Investigation of multispectral imaging algorithm for temperature determination on a numerical experiment platform in Laser-based Powder Bed fusion of Metals

Author:	B.Sc. Zhaoyong Wang	**Supervisor:**	M.Sc. Ruihang Dai
Issuance:	15.03.2023	**Submission:**	31.12.2021

Setting:
Laser-based Powder Bed Fusion of Metals (PBF-LB/M) is an additive manufacturing process which produces components with a laser by successively melting metal powders applied in layers. This additive manufacturing process offers the advantage of a complex lightweight design. However, complicated thermal histories during laser-metal interaction can lead to process defects such as keyholing. Since the process is thermally driven, acquiring the absolute temperature distribution in the laser-material interaction zone is vital to gain a deeper understanding of the process. However, no measurement system in PBF-LB/M is currently available to determine the absolute temperature due to unknown emissivity. Multispectral Imaging (MSI) has the potential to determine the absolute temperature and emissivity simultaneously by capturing multiple wavelengths of radiance from the melt pool.

Objective:
This work aims to optimize the MSI algorithm to determine the absolute temperature accurately. Since the mapping between the digital value and radiance still needs to be investigated, direct optimization of the MSI algorithm based on the experimental data is challenging. Therefore, the first step is to develop a virtual experiment to obtain "ideal" radiance determined by the given temperature distribution and emissivity. This way, the MSI algorithm can be optimized based on the input and calculated temperature and emissivity. The virtual experiment platform will also allow for the investigation of various temperature distributions and emissivity models in a time- and cost-efficient manner.

Methodology:
The content of the present thesis can be subdivided into the following tasks

- Literature review regarding MSI, material emissivity model and curve fitting algorithms
- Development of a virtual experiment platform
- Generate virtual experiments with various emissivity models and temperature fields
- Optimization of the MSI algorithm based on virtual experiments
- Scientific documentation of the results

Declaration

I hereby confirm that this semester thesis was written independently by myself without the use of any sources beyond those cited, and all passages and ideas taken from other sources are cited accordingly.

.....	.....
Location, Date	Signature

With the supervision of Mr. Zhaoyong Wang by Mr. Ruihang Dai intellectual property of the Professorship Laser-based Additive Manufacturing (LBAM) flows into this work. A publication of the work or a passing on to third parties requires the permission of the head of the professorship. I agree to the archiving of the printed thesis in the LBAM library (which is only accessible to LBAM staff) and in LBAM's digital thesis database as a PDF document.

.....	.....
Location, Date	Signature

Abstract

temperature is one of the most important parameters in PBF-LB/M. so, monitoring the temperature at melt pool necessary. in oder to archieve this, a numerical experiment platform is formed. then parameter is calculated

Zusammenfassung

Hier könnte Ihre Kurzzusammenfassung stehen.

Contents

1 Introduction

Additive Manufacturing (AM) is a different type of processing technology to conventional manufacturing methods. Instead of removing material from the raw part, additive manufactoring is usually described as "a process of joining materials to make objects layer by layer or element by element"[1]. It is a useful method for reducing the the duration from product design to product manufacturing and imporving the material utilization[2].

There are several AM technologies that can be sorted into different categories. Laser-based Powder Bed Fusion of Metals (PBF-LB/M), which also called Selective Laser Sintering (SLS), is one of the powder based AM processes[3]. In this process, a laser beam with high energy density is focused onto the surface of a metal powder bed, which was heated up to a temperature near the melt temperature. Then, the metal powder is melted and form the upper surface of the object. Last, the building platform will go downwards to build next layer. This process will be repeated until the desired object is built[4].

Since the process is based on the phase change of materials, processing parameters such as laser power, layer thickness, hatch distance and scanning strategies are critical for producing dense materials, minimize defects, improve surface quality and build rate[5]. The common denominator between them is that the parameters of the process are varied by controlling the temperature profile of the metal powder[2]. Thus, the importance of obtaining the temperature information on the surface layer is high.

The solidification front of metal powders moves with a high velocity (generally $0.01 \sim 10\,\mathrm{m/s}$)[6], the cooling rate of material is normally at range of $10^5 \sim 10^6\,\mathrm{K/m}$[5]. Thus, a contactless temperature measurement is required to obtain the temperature of the surface area.

Two different methods is used for monitoring the surface temperature in recent studies, namely conventional infrared irradiation temperature measurement methods and multi-wavelength techniques[7]. Infrared irradiation technique is cost-effective, but it requires information about the emissivity of the material[8]. On the contrary, a multi-color pyrometer with a specific wavelength range could be used in the case of changing emissivity[9]. In this thesis, a virtual experiment platform using a multispectral imaging algorithm is developed to simulate the output behavior of a spectral pyrometer.

After obtaining the radiation image, a curve fit algorithm is applied to estimate the temperature field of the image and emissivity field simultaneously. This semester thesis aims to develope a stable temperature estimation program based on curve-fit algorithm. With the results obtained from the virtual experiment platform, the performance of the temperature estimation algorithm is verified.

2 State of the art

AM has undergone significant advancement since its inception 25 years ago[10]. Presently, AM has achieved widespread utilization across industries including aerospace and dentistry. It demonstrates versatile capabilities for processing materials like metals, ceramics, polymers as well as composites[1]. Many researchers have classified these processing techniques into the following categories[3], [11]:

- Vat Photopolymerization (VPP)
- Material Jetting (MJT)
- Binder Jetting (BJT)
- Material Extrusion (MEX)
- Powder Bed Fusion (PBF)
- Sheet Lamination (SHL)
- Direct Energy Deposition (DED)

Each process possesses its own advantages and disadvantages, contingent upon factors such as the materials being processed, construction speed, dimensional accuracy, etc[11].

In this work, the primary focus is the monitoring process in PBF-LB/M. Hence, in this chapter, the PBF-LB/M technology will be introduced, followed by an exploration of the monitoring methods employed in contemporary PBF-LB/M. Among these methods, multispectral imaging has been selected as the monitoring technique utilized in this work. Consequently, this establishes the underlying principles of the observation aspect within PBF-LB/M. Subsequently, the material's emissivity model will be introduced, thus leading to the current temperature estimation algorithms in use.

2.1 Laser-based Powder Bed Fusion of Metals

In 1989, Carl Deckard and Joe Beaman pioneered a technique SLS. Within this methodology, high-energy density lasers are focused onto the surface of metal powder, resulting in the formation of a solidified metal layer[12], [13]. In the year 2002, Fisher et al. observed a phenomenon of partial melting in metal powders. This discovery led to the potential reduction of porosity in components produced through the original SLS process, subsequently enhancing the mechanical properties of the materials. However, it should be noted that complete elimination of porosity remains unattainable within the partial melting sintering methodolgy[14].

With the development of laser technology, the utilization of partial melting in SLS has been supplanted by the Selective Laser Melting (SLM) approach. Within this technique, metal powder is subjected to complete melting, resulting in an elevated density of the produced part. However, the heightened thermal gradient inherent in this method gives

rise to internal stresses within the finalized components[15], necessitating heat treatment to alleviate these effects[16].

Laser-based Powder Bed Fusion (PBF-LB) is a type of AM process that uses a laser beam to selectively melt and fuse metal powder layers according to a digital model[17], which includes SLS and SLM. The structure of the PBF-LB/M machine can be found in Fig.1.

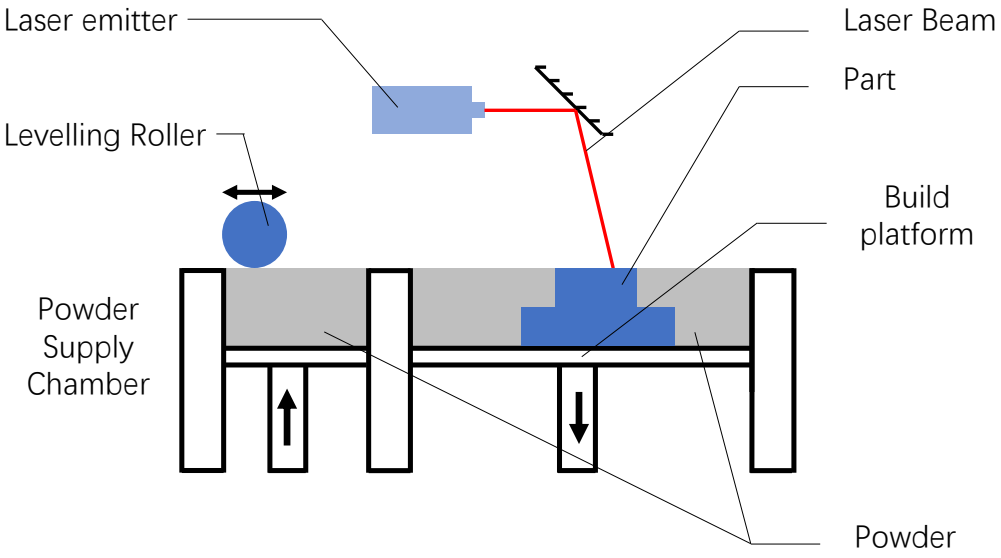

Figure 1: Laser-based Powder Bed Fusion of Metals

Oliverira et al. [5] have highlighted that two key operational parameters exist within the context of PBF-LB/M: the source power and the scanning velocity. These two parameters exert an influence on the energy density imparted to the metal powder, consequently affecting the resulting porosity of the fabricated product. Meanwhile, porosity stands as a critical parameter impacting the performance of the final product. The researchers [5] have categorized the porosity of the finished product into four distinct classes:

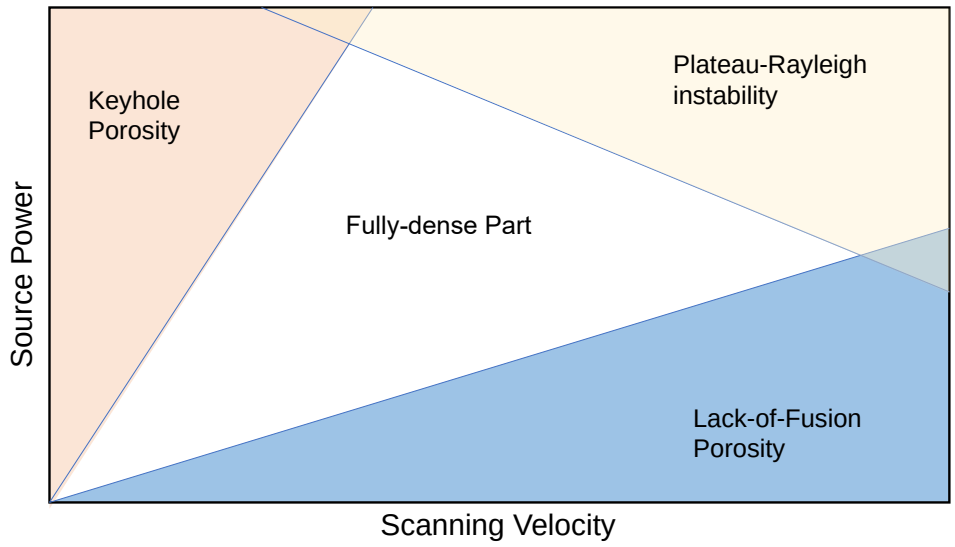

Figure 2: Influence of process parameter on porosity. Reproduced from [5]

- Keyhole Porosity: Excessive energy density inhibits the conduction of the melt pool on the powder bed, leading the melt pool to transition into a keyhole mode.
- Lack-of-Fusion Porosity: Insufficient energy density results in incomplete fusion of the metal powder, leading to the formation of porosity.
- "Balling" (Plateau-Rayleigh instability): Simultaneously employing high source power and excessively elevated scanning velocity induces instability during the processing operation.
- Fully-dense porosity: The ideal energy density enables the component to attain a fully dense part.

Matthews et al. [18] pointed out that in order to determine the evolution of the material's microstructure, information such as cooling rate, thermal histories, and material properties are imperative. This underscores the necessity of monitoring the PBF-LB/M process.

2.2 Process monitoring

Li et al. [7] emphasized that in-situ temperature measurement is of significant importance for characterizing the mechanical properties of materials. In-situ temperature measurement can be categorized into in-contact technique and non-contact technique. Given that the temperature of the material is high (exceeding 1000°C), the region being heated by laser is small, and the cooling rate as well as the heating rate is high, contact-based measurements would encounter substantial interference, thereby rendering the obtained temperature information unreliable. Consequently, it becomes essential to employ non-contact-based temperature measurement methods.

In the realm of non-contact temperature measurement, various measurement systems encompassing ultrasonic, acoustic, and optical techniques are present. Within the context of PBF-LB/M, optical sensors are extensively utilized[19].

Mani et al. [20] pointed out that thermographic imaging in the context of Additive Manufacturing (AM) can be classified into two categories based on the optical pathway of the imaging system. One category involves aligning the field of view of the sensor with the laser beam[21]–[27].

Fig.3 presents the structure of the measurement system. This alignment enables the field of view to track the laser beam, allowing for the observation of the melt pool and its scan trajectory. In addition, an alternative approach involves placing the sensor independently of the laser beam. This configuration enables the field of view relative static to the material[22], [28]–[32]. In this work, due to the use of an observation system independent of the laser beam in the actual experiments, the virtual experimental platform also features a sensor separated from the laser beam system. This setup facilitates system calibration and allows direct acquisition of sensor parameters such as quantum efficiency.

Ueda et al. designed the first infrared pyrometer (single-wavelength temperature measurement) to measure the temperature. This approach relies on the principles outlined in Planck's law, which delineates the interplay between temperature, wavelength, and radiative intensity, enabling the measurement of the temperature of the object[33]. Subsequently, Dinwiddie et al. applied this method for temperature measurement in electron beam melting[28]. Meanwhile, Krauss et al. employed this technique to identify defects and discontinuous failure spots arising during the AM process[19].

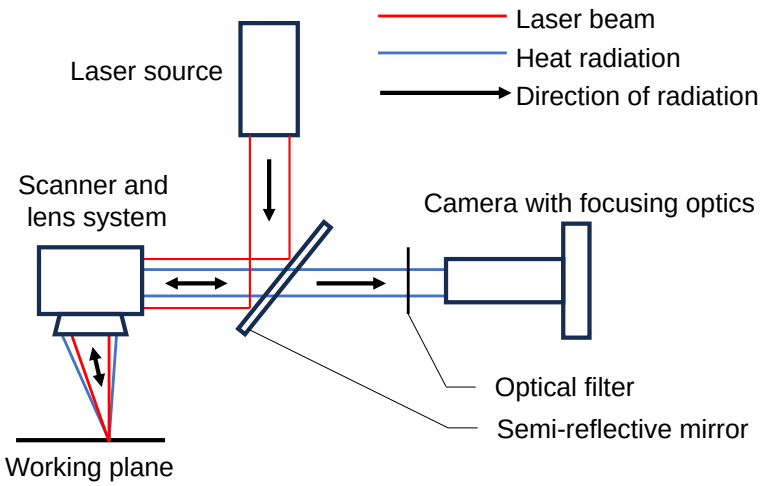

Figure 3: System structure of co-axial monitoring system based on [21]

However, due to the intricate nature of temperature in real cases, the single-wavelength temperature measurement approach may lead to misrepresentations of temperature measurement. The models employed in single-wavelength temperature measurement methods lack appropriate parameters, rendering them susceptible to interference and unable to accurately depict the phenomenon of changing emissivity with increasing wavelength[34].

Subsequently, the emergence of multiwavelength pyrometers became notable. In this technique, the intensity of radiation at two or more wavelengths is measured during the processing. Doubenskaia et al.[35], Smurov et al.[36], and Muller et al.[37] have achieved measurement of the melt pool using this approach. However, in their methods, knowledge of emissivity variation with wavelength is required, which is often unknown. This necessitates assuming a material to be a grey body, which that can lead to inaccuracies in temperature calculations.

Meanwhile, the multiwavelength pyrometer is limited to measuring the temperature at a specific point. For certain applications, the temperature distribution is crucial, such as detecting local hot spots and cold spots, as well as assessing the temperature distribution of the materials mentioned in this work. Consequently, the utilization of methods with enhanced spatial resolution becomes imperative[38]. To enhance the spatial resolution of temperature measurement, measurement systems based on cameras have been developed. These systems are primarily categorized into multispectral imaging and hyperspectral imaging. The distinction between them lies in the wavelength range that the sensor can capture. In multispectral imaging, the sensor receives discrete wavelengths, while in hyperspectral imaging, the sensor detects a continuous range of wavelengths[39]. In this work, multispectral imaging was employed as the technique for temperature measurement.

2.3 Multispectral imaging

In order to simultaneously acquire radiation information at different wavelengths, a beam splitting design is deemed essential. Spering et al. have pioneered a patented approach for achieving beam splitting through the utilization of a series of spectral filters[40]. As shown in Fig.4, within this system, radiation of varying wavelengths is directed towards

different sensors. Subsequently, these sensors receive the radiation information, which is then amalgamated into a composite image through post-processing techniques. However, due to the necessity of radiation to traverse multiple layers of spectral filters, it becomes impractical to increase the number of observation channels without compromising the overall system performance.

With the development of camera manufacturing technology in the 1970s, the fabrication of single-pixel-level spectral filtering became feasible[42]. Hagen et al. noted that due to the placement of all spectral filters on the detection layer, this design exhibits a highly compact configuration. However, this also introduces a drawback, necessitating the image to be spatially bandlimited to the Nyquist limit of the filter array. Failure to adhere to this requirement results in the presence of aliasing effects in the acquired images. Such effects can be mitigated by defocusing the image, thereby reducing the impact of the bandlimit constraint[41].

Due to its low utilization costs and intuitive data representation, the camera in the virtual experimental platform of this work employs this technique.

2.4 Emissivity model

The previous section highlights the significant influence of a material's emissivity on the actual radiative emissions it emitted, which directly impacts the accuracy of data obtained through sensors. Jones et al. underscore that the emissivity of all materials varies with temperature and wavelength[43]. Therefore, it is imperative to conduct observations of a material's emissivity.

Numerous researchers have conducted experimental research on the emissivity of various materials. Hagqvist et al. employed a narrow bandwidth spot radiation pyrometer along with a calibration procedure to estimate the spectral emissivity of Ti–6Al–4V[8]. They utilized a virtual pyrometer for measuring the reference temperature T_r. The material's emissivity at the reference temperature could be considered as known. By comparing the values obtained from the actual pyrometer and the virtual pyrometer, the measured emissivity values could be derived.

Jones et al. conducted measurements of the total normal emissivity $\varepsilon(T)$ of some materials at high temperature[43]. They employed a blackbody material as a reference during these measurements.

$$\varepsilon(T) = \frac{\int_{\lambda_1}^{\lambda_2} \varepsilon(\lambda, T) \cdot I_b(\lambda, T)\, d\lambda}{\int_{\lambda_1}^{\lambda_2} I_b(\lambda, T)\, d\lambda} \tag{2.1}$$

In their experiments, it was demonstrated that factors such as material temperature, purity, composition and surface quality significantly influence the total normal emissivity of the materials.

In the emissivity measurement of 309S steel conducted by Zhu et al., it was noted that the oxide layer also exerts a significant influence on the emissivity[44].

Hence, it can be inferred that obtaining accurate emissivity information of the material is challenging. This is especially diffcult for the metallic powders utilized in the present work. Consequently, performing real-time emissivity estimations for the material becomes essential within the scope of this work.

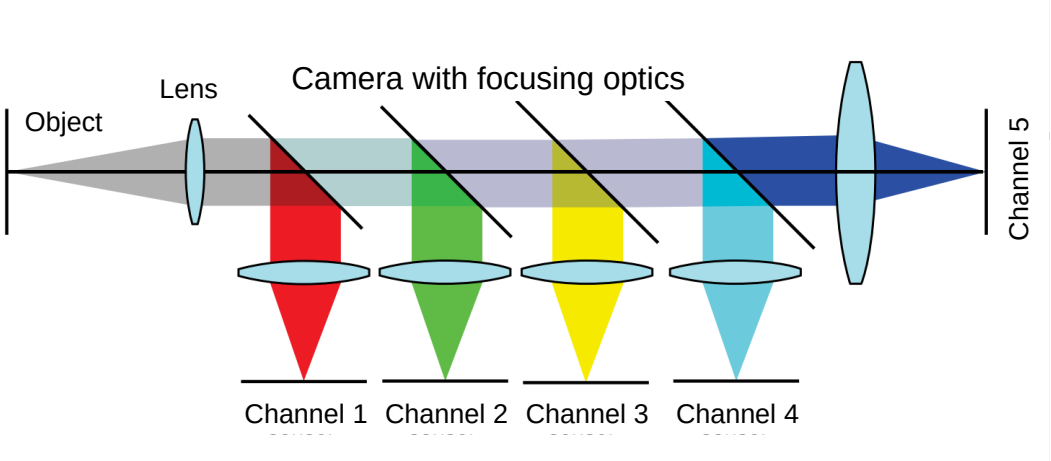

Figure 4: Beam splitting structure from Spiering et al. Reproduced from [41]

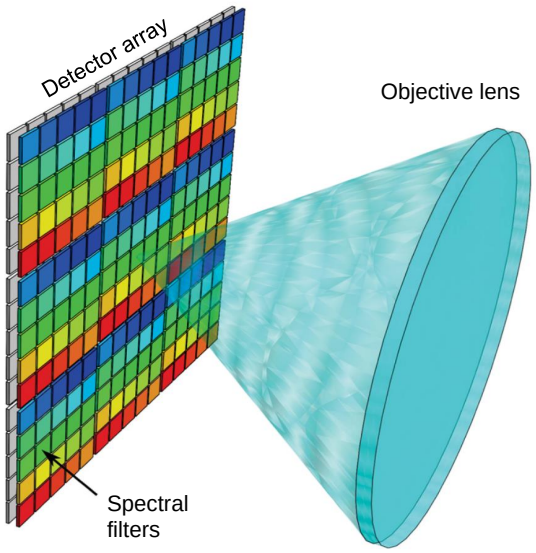

Figure 5: System layout of a pixel-level filter. Reproduced from [41]

Kobatake et al.[45], Watanabe et al.[46] and Krishnan et al.[47] conducted measurements of the emissivity of liquid iron and nickel. They observed a decreasing trend in the emissivity of liquid iron with increasing wavelength. Notably, Kobatake et al. also measured the emissivity of iron at different temperatures specifically at a wavelength of 807nm.

From this, it becomes evident that directly measuring the spectral emissivity of materials at different temperatures presents challenges. In order to facilitate numerical experiments, Taunay et al.[48] and Wang et al.[49] developed hypothetical emissivity models. Within these simulated emissivity models, material characteristics can be manually adjusted to assess the accuracy of the system when dealing with various radiative properties of materials.

Consequently, the virtual experimental platform employed in this work conducted calculations based on the proposed hypothetical materials. This approach serves to save the time cost associated with measuring the spectral emissivity of actual materials at various temperature.

2.5 Temperature estimation algorithm

Having gobtained the emissivity model of the material, temperature estimation algorithms should be employed for calculating the material's temperature as well as emissivity simutaneously.

In the dual-wavelength pyrometry, researchers introduced an assumption that the material's emissivity remains constant at two wavelengths of the channels. This assumption directly eliminates the impact of emissivity on temperature calculations[38].

$$\widehat{T}(\lambda_i, \lambda_j) = C_2 \frac{1/\lambda_j - 1/\lambda_i}{ln(I_i/I_j) - 5ln(\lambda_j/\lambda_i)} \tag{2.2}$$

Devesse et al. pointed out that such simplification does not align with the actual characteristics of materials and can lead to inaccuracies in temperature calculations[39]. Therefore, they proposed a linear emissivity model based on the trend of decreasing emissivity with increasing wavelength for metals.

$$\varepsilon(\lambda, A_\varepsilon, B_\varepsilon) = B_\varepsilon - \frac{A_\varepsilon}{2} \cdot \lambda \tag{2.3}$$

This allowed them to reconstruct the radiative intensity received by the sensor using this emissivity model. By adjusting the parameters A_ε and B_ε, this method can attain the desired emissivity model.

There are also a number of methods that utilize different approaches for temperature estimation as alternative. Wang et al. developed a constraint optimization algorithm that operates independently from the emissivity model[49]. They introduced an objective function $f(x)$ as follows:

$$f = \frac{1}{n} \sum_{n=1}^{n} \left(T_i - \overline{T}_E \right)^2 \tag{2.4}$$

Where T_i is computed based on the radiative intensity I_i received from the i_{th} channel and $\overline{T}_E$ is the average value of T_i:

$$T_i = \frac{C_2}{\lambda_i}\left(ln\varepsilon_i + ln\frac{C_1}{\lambda_i^5} - lnI_i\right)^{-1} \tag{2.5}$$

Subsequently, constraints were established based on the fact that emissivity decreases with increasing wavelength. A genetic algorithm was employed to determine the emissivity and temperature that minimize the objective function. This process led to the estimation of temperature and emissivity. This approach enables the program to compute emissivity data of the material without requiring an emissivity model. However, due to the structure of the program, it can only obtain the material's emissivity at specific wavelengths.

Taunay et al. developed a temperature estimation method based on multi-wavelength pyrometry[48]. In this approach, an estimated temperature $\widehat{T}(\lambda_i, \lambda_j)$ is obtained by utilizing the radiative intensity from two distinct channels (λ_i, λ_j):

$$\widehat{T}(\lambda_i, \lambda_j) = C_2 \frac{1/\lambda_j - 1/\lambda_i}{ln(I_i/I_j) - 5ln(\lambda_j/\lambda_i) - ln(\varepsilon_i/\varepsilon_j)} \tag{2.6}$$

After obtaining a series of estimated temperatures $(\widehat{T}(\lambda_i, \lambda_j))$, the average of all the estimated temperatures is taken as the output result of the system T_0.

$$T_0 = \frac{1}{N_T}\sum_{i=1}^{N-1}\sum_{j=1}^{N}\widehat{T}(\lambda_i, \lambda_j) \tag{2.7}$$

It is evident that this model necessitates an accurate emissivity model for the material. Moreover, during temperature estimation[48], the computational complexity increases notably with an escalation in the number of channels.

2.6 Motivation of this thesis

In summary, there is significant room for development in using multispectral imaging methods for temperature estimation in the context of PBF-LB/M.

Firstly, real-world experiments are often affected by various non-ideal factors such as material surface reflections and sensor placement, which can negatively impact the experimental outcomes. Additionally, the sensors themselves might capture undesirable noise signals during data acquisition. In practical experiments, the performance of temperature estimation algorithms can be compromised by these adverse effects.

Secondly, the complete characterization of the material properties under test is challenging. As mentioned earlier, the emissivity of a material is influenced by various factors such as temperature, wavelength, surface quality, degree of oxidation, and composition, etc. Particularly for the metallic powders used in PBF-LB/M, obtaining precise emissivity data for the material poses challenges. Moreover, in the use case, the laser beam rapidly moves across the surface of the metallic powder, leading to high temperature gradients and changing rates. This makes it impractical to validate the accuracy of temperature estimation algorithms under real use case conditions.

Lastly, previous research has often ignore the non-idealities of the sensors. In the case of a multispectral camera with pixel-level filters, these filters are not ideal, as they only receive radiation at their nominal wavelengths. In contrast, these channels allow radiation

within certain wavelength ranges to pass through, causing a deviation between the measured digital value and the actual radiation intensity reaching the sensor surface. Simultaneously, there exists cross talk between different filters, leading to a lower peak in the quantum efficiency of the sensor at different wavelengths. These factors result in a discrepancy between the information obtained from the sensor and the actual conditions, necessitating a novel post-processing approach to achieve temperature and emissivity estimation functionalities.

Consequently, this work introduces a novel virtual experimental platform. Within this platform, experiment data of hypothetical materials without interference can be generated based on specific parameters such as temperature distribution and emissivity model. Subsequently, temperature estimation algorithms use this experimental data to compute the temperature and emissivity of the simulated test materials. Since the emissivity characteristics and temperature of the hypothetical materials are known, this allows for an evaluation of the performance of the temperature estimation algorithms in terms of accuracy and consistency. This approach thus opens up greater potential for enhancing the performance of temperature estimation algorithms.

3 Theory and methodology

As mentioned in previous sections, forming a virtual experiment platform is necessary for investigating the temperature estimation algorithm. So, a virtual experiment platform is developed based on Planks'law, then, a virtual multi-spectral pyrometer is applied to obtain the digital value (also called image).

3.1 Physical value of radiation

Radiation is emitted from any object with a temperature above 0 K. In equation 3.1 can be found, that the radiation depends on the black body radiation $B(\lambda, T)$ and emissivity $\varepsilon(\lambda, T)$. Both value are temperature T and wavelength λ dependent.

$$L(\lambda, T) = B(\lambda, T) \cdot \varepsilon(\lambda, T) \tag{3.1}$$

By Plank's Law, black body radiation can be described in Eq.3.2,

$$B(\lambda, T) = \frac{2hc^2}{\lambda^5} \cdot \left[\exp\left(\frac{hc}{\lambda k_B T} \right) - 1 \right]^{-1} \tag{3.2}$$

With absolute temperature T, wavelength λ, speed of light c, Plank constant h and Boltzmann constant k_B. Black body radiation is irrelevant to the material itself, all materials at the same temperature have the same spectral black body radiation.

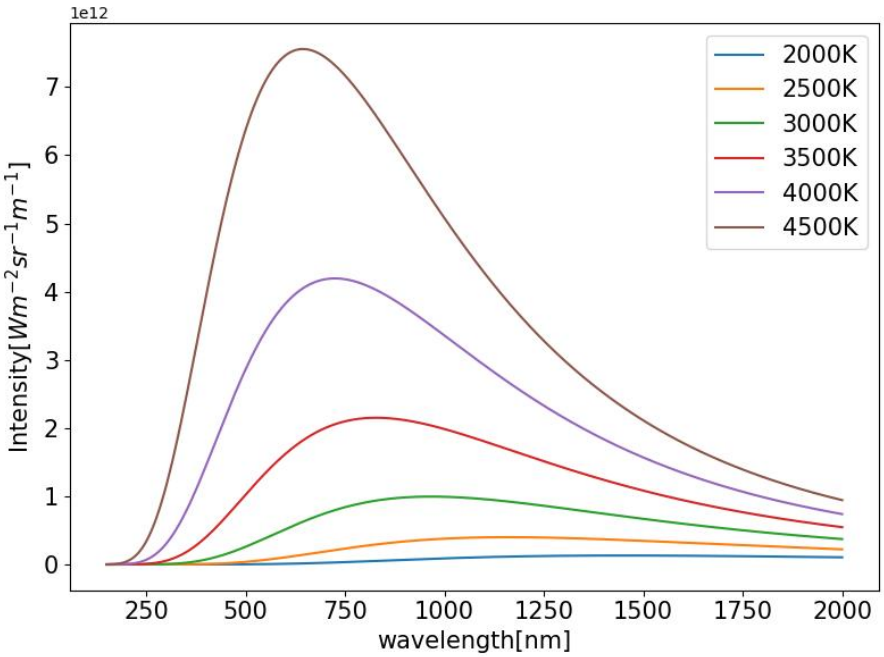

Figure 6: Black body radiation of materials with different temperature

Fig.6 illustrates the spectral radiation intensity of a blackbody at different temperatures. It can be observed that the spectral radiation intensity exhibits a peak at a specific wavelength.

According to Wien's displacement law, the relationship between the wavelength of the peak λ_{peak} and temperature T can be described in Eq.3.3:

$$\lambda_{peak} = \frac{b}{T} \tag{3.3}$$

With Wien's displacement constant $b = 2898\mu m \cdot K$, it can be found that the wavelength of this peak decreases as the temperature rises.

From this, it can be concluded that the shape of the blackbody's spectral radiation intensity varies with temperature. This is evident in two aspects: firstly, the position at which the peak appears, and secondly, the distribution of spectral radiation intensity along the wavelength. Indeed, this characteristic provides the possibility to determine the temperature of a blackbody material in reverse, i.e., by calculating the temperature based on the known spectral radiation intensity.

On the contrary, emissivity varies from material to material. It is the ratio of the actual spectral intensity emitted by the object to the spectral intensity of the black body radiation. In the study of radiation, two idealized material models are generally used to describe the idealized properties of radiation, namely black body and grey body.

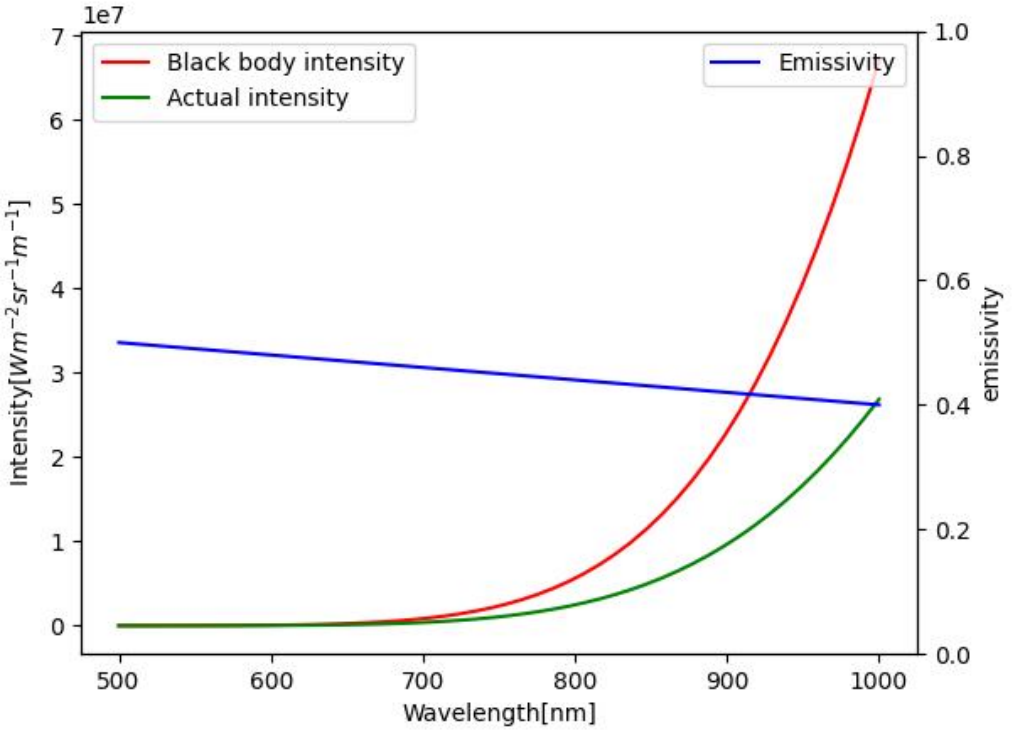

Figure 7: Black body radiation, emissivity and real radiation of an example normal material at $1000K$

Black-body material emits electromagnetic black body radiation, which is irrelevant to the wavelength of the radiation and the shape of the material[50]. Which also means the emissivity of a black body is constantly 1. It could be used to validate the temperature estimation algorithm in following sections.

Unlike black-body materials, grey-body materials have an emissivity between 0 and 1. Not all of the thermal radiation could be emitted to the outside of the material. Different from

normal materials, the emissivity of a grey-body material is irrelevant to the wavelength of radiation.

In Fig.7 can be found, that the real spectral intensity of a normal material is lower than the black body spectral intensity. And the emissivity of the material varies with the increase of the radiation wavelength.

It can be seen that the construction of a reliable emissivity model is crucial to the accuracy of the virtual experimental platform. It is the key component used to generate the experimental data.

3.2 Virtual experiment platform

After obtaining the physical spectral intensity of the material, a virtual experiment platform is used to transform the physical value into digital value, which simulate the behavior of a real spectral pyrometer. As described in Fig.8a, a camera with a lens system focused on the surface of the powder bed is resonsible for obtaining spectral radiation of the heated metal powder. It can be seen from Fig.8b, each pixel of the sensor contains 8 filters and thus be able to obtain 8 intensity digital values in different channels. Thus, a virtual experiment platform with the same structure as the real experiment platform is built.

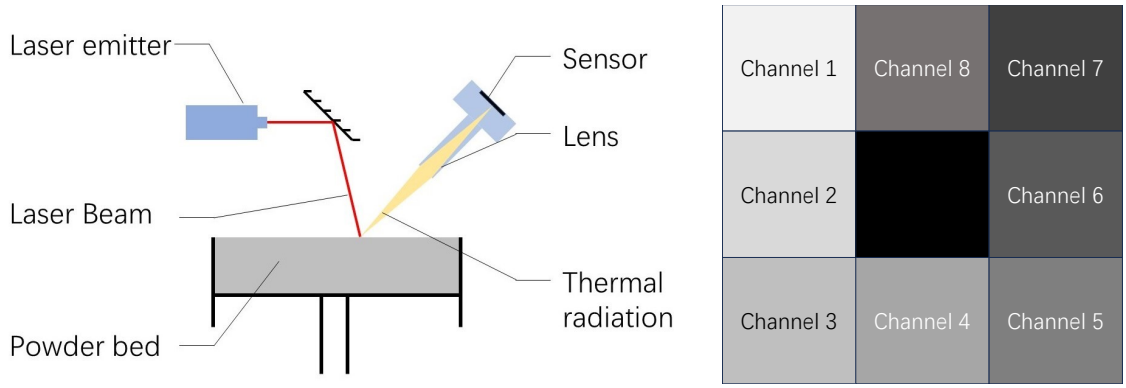

(a) Virtual experiment platform (b) Layout of a sensor pixel

Figure 8: Structure of the virtual experiment platform and Layout of a sensor pixel

3.3 Camera model

It can be found in Fig.8, The thermal radiation is emitted from the surface of powder bed, and passes through the lens system of the camera, finally, it reaches the sensor and be converted into digital values. The simplified process can be seen in Fig.9. As dA_m is the area of the focused surface and dA_{pixel} the area of the pixel in camera system, n_m is the normal vector of the surface.

3.3.1 Frequency response

After obtaining the virtual experiment platform and knowing the external setup of the sensor, the internal effects of the camera system should also be taken into account in the complete virtual experiment platform.

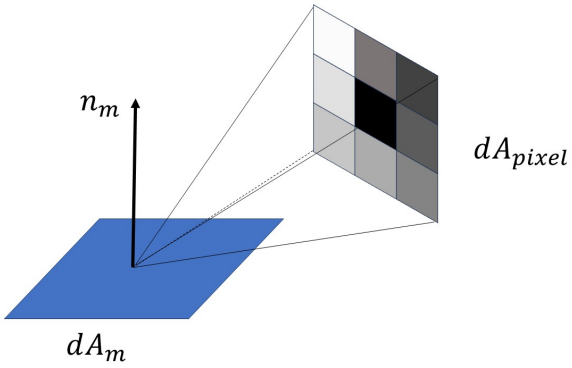

Figure 9: Radiative exchange between camera system and powder bed

In order to simulate real camera system, the frequency response of sensor and lens should be considered. In real camera systems, all spectral radiation will pass through the lens system of camera. Since the lens system is not an idealized system, the effect of the lens system is not negligible.

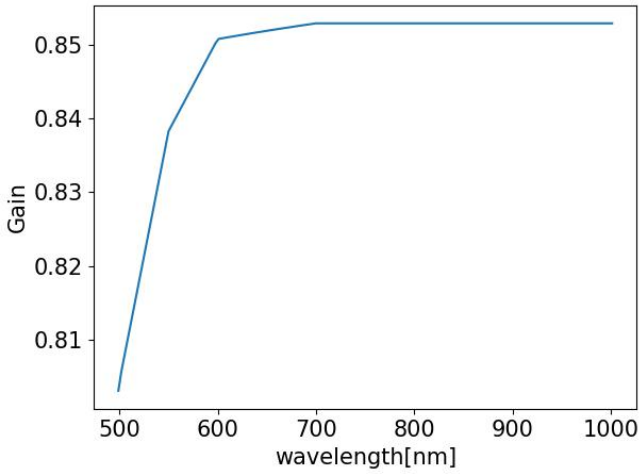

Figure 10: Frequency response of the lens system

It can be found in Fig.10 that system gain of lens system is not constant. In the wavelength range of 500 to 700 nanometers, the lens is more sensitive to the radiation with long wavelength. With the increasing wavelength, the system gain of the lens system keep constant at 0.853.

In addition to the fact that the lens system respond differently to radiation with different wavelengths, the sensor of the camera also have wavelength-dependent quantum efficiency. As mentioned in previous section, the acquisition of the spectral intensity by the sensor for different channels is based on the filter before the pixels.

Fig.11 shows the quantum efficiency of the camera sensor in different channels. Unlike an ideal sensor that receives only single wavelength radiation, the intensity information received by a real sensor is a combination of a spectral radiation and 8 filters with different frequency responses. Thus, the camera system is able to obtain the spectral radiation intensity in 8 channels simutaneously.

To make the virtual experiment platform more comparable to real experiments, it can be

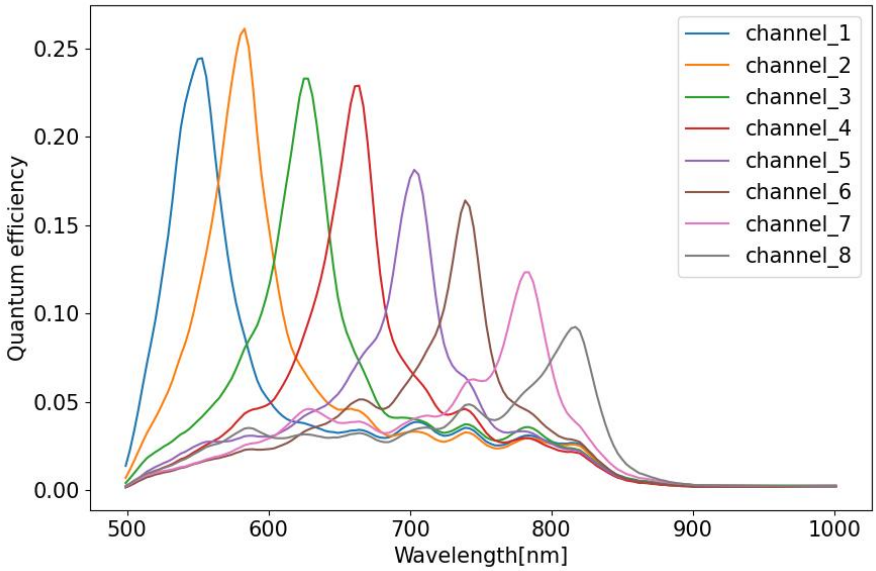

Figure 11: Quantum efficiency of camera system in each channel

concluded that it is necessary to build a camera model that incorporates the effects of sensor quantum efficiency and lens transparency. Then, the physical value of the spectral radiation intensity could be calculated accurately by the digital value of spectral radiation intensity obtained from the virtual experiment platform.

3.3.2 Integration method

As a result, the process of converting the physical values of radiation intensity into digital values needs to be accurately reproduced. Since the total efficiency of the camera (η_{camera}) was delivered by quantum efficiency ($\eta_{quantum}$) of the sensor and transparency of the lens system (τ_{lens}), the mathematical relationship could be described in Eq.3.4.

$$\eta_{camera} = \eta_{quantum} \cdot \tau_{lens} \tag{3.4}$$

Fig.12 shows the relationship between the incoming spectral radiation intensity and actual captured spectral radiation intensity by the camera system. It can be found that the wavelength of the spectral radiation intensity actually received by the sensor deviates from the wavelength of the spectral radiation intensity it supposed to receive.

Obtaining the physical value of spectral radiation intensity, the sensor is responsible for transforming the physical value into digital value for upcoming proceedings. The camera system used in real experiment platform uses Charge-coupled device (CCD) or Complementary Metal-oxide Semiconductor (CMOS) as their sensors. Both sensors transform the photon flux $\phi(\lambda)$ incident on the semiconfuctor into photocurrent I_{ph}[51].

$$I_{ph} = q \int_{\lambda} \phi(\lambda) \cdot \eta_{camera}(\lambda) d\lambda \tag{3.5}$$

With a certain temperature T:

$$\phi(\lambda) = L(\lambda, T) \tag{3.6}$$

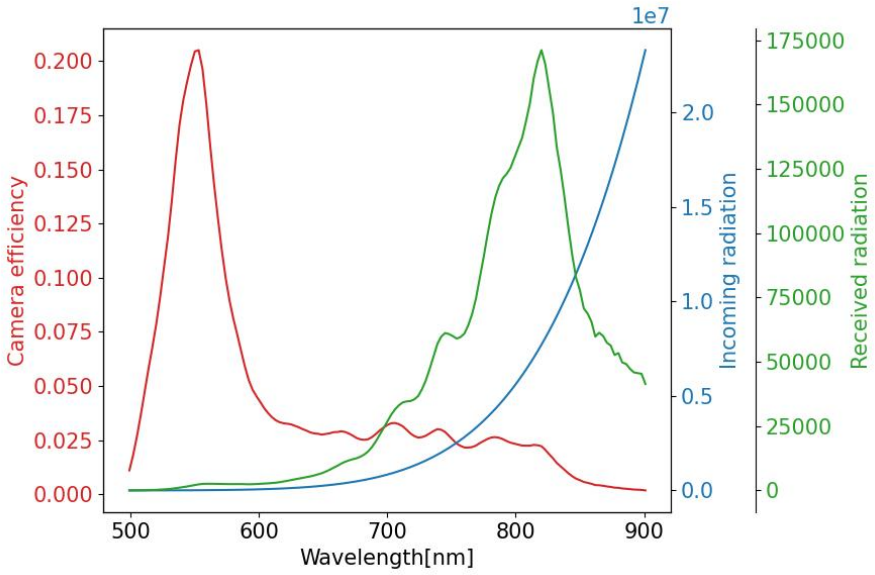

Figure 12: Actual received spectral radiation intensity by channel 1 at 1000K

Eq.3.5 is the mathetical description of the transformation. Where $\phi(\lambda)$ denotes photon flux on the sensor, which is equal to the spectral radiation intensity on the sensor $L(\lambda, T)$ as described in Eq.3.6, and $\eta_{camera}(\lambda)$ denotes the total efficiency of the camera in Eq.3.4. q is the sensitivity parameter of the sensor.

3.3.3 Implementation

Similar to the method used to obtain the digital value of spectral radiation intensity in the real experiment, the virtual experiment platform calculates the intensity digital value in 8 channels using the virtual camera by entering the material properties of the point being measured.

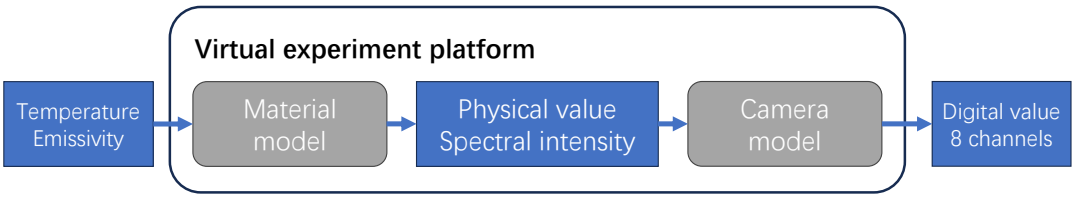

Figure 13: Procedure of using virtual experiment platform to generate digital values

Fig.13 shows the working procedure of the virtual experiment platform. To enable the virtual experimental platform to run on various devices, the entire platform has been implemented using Python as the programming language and packaged into a .py file. Furthermore, all functions have been vectorized to facilitate the generation of image outputs resembling those captured by a physical camera. Additionally, the parallel computing package in Python has been utilized to minimize computation time.

3.4 Temperature estimation algorithm

After obtaining the experimental data calculated by the virtual experiment platform, a temperature estimation algorithm should be developed to calculate the temperature of the measured point based on the experimental data.

Similar to the set up in real experiments, the parameters of the camera model can be considered as known in the virtual experimental platform mentioned in this article. This will on the one hand improve the accuracy of the temperature estimation algorithm and on the other hand avoid some unnecessary complexity.

Thus, in this temperature estimation algorithm, the known variable is the digital value of spectral intensity captured by camera model in virtual experiment platform, the characteristic of the camera system. The variables to be estimated are the temperature of the measured point and its emissivity.

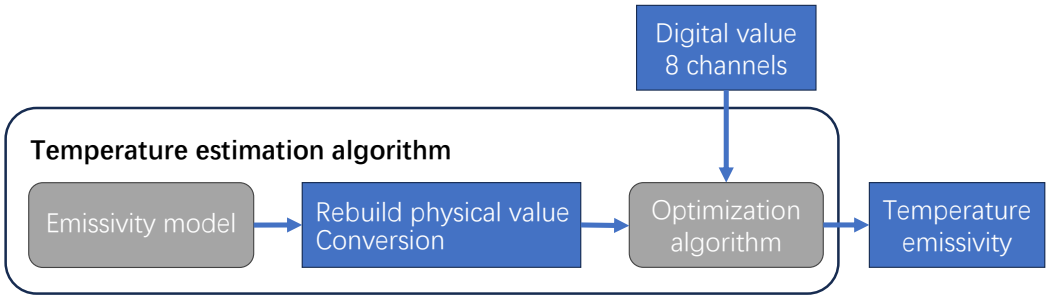

Figure 14: Procedure of temperature estimation algorithm

Fig.14 shows the proceeding procedure of the temperature estimation algorithm. The physical value of the spectral radiation intensity ($I_{rec}(i)$) in the i_{th} channel should be reconstructed in Eq.3.7:

$$I_{rec}(i) = q \int B(\lambda, T) \cdot \varepsilon(\lambda, k, T) \cdot \eta_{camera}(i) d\lambda \tag{3.7}$$

With $I_{rec}(i)$ the reconstructed physical value in i_{th} channel, $B(\lambda, T)$ the black body radiation, $\varepsilon(\lambda, k, T)$ the emissivity model in temperature estimation algorithm, $\eta_{camera}(i)$ the total camera efficiency of i_{th} channel. It can be found that the emissivity model have an additional parameter k, this parameter is used for fitting the emissivity behavior of the measured material. More details can be found in the following section.

Once the reconstruction of the physical value is completed, it is necessary to convert this physical value into a digital value. This conversion process is dependent on the parameter settings of the sensor system, such as exposure time, aperture size of the lens, etc. For the purposes of this paper, it is assumed that the conversion relationship is linear.

Given an initial guess of the status parameters, namely temperature(T_0) and parameters in emissivity model(k_0). Then, an curve fit algorithm is applied to minimize the difference between the reconstructed digital value (I_{rec}) and the actual digital value (I_{act}) in Eq.3.8.

$$\min_{k,T} \sum_{i=1}^{8} F(I_{rec}(i), I_{act}(i)) \tag{3.8}$$

$F(I_{rec}(i), I_{act}(i))$ is the cost function of the curve fit algorithm. In this application, Non-linear least squares method is used to obtain the optimum parameters as Eq.3.9.

$$F(I_{rec}(i), I_{act}(i)) = (I_{rec}(i) - I_{act}(i))^2 \tag{3.9}$$

After obtaining the estimated temperature ($T_{estimate}$) and the parameter (k) in the emissivity model, the data will be saved in a .xlsx file for potential operations.

3.5 Emissivity model in temperature estimation algorithm

As an unknown quantity in the temperature estimation algorithm, the nature of emissivity as a function of wavelength also introduces an additional degree of freedom into the overall calculation process. In order to provide a more general description of the trend of emissivity with wavelength, an additional parameter (k) in the emissivity model used for temperature estimation has been introduced.

Due to the inherent complexity of this trend, it is often impossible to describe the emissivity using a single parameter. Therefore, the parameter (k) is normally represented as a vector composed of multiple variables. This approach allows for both a concise mathematical representation and the incorporation of more intricate emissivity models into the temperature estimation algorithm.

4 Approach

After the theoretical basis of the virtual experiment platform is known and the program of the virtual experiment platform is built, the application should be verified with experiment data generated based on the real experiment.

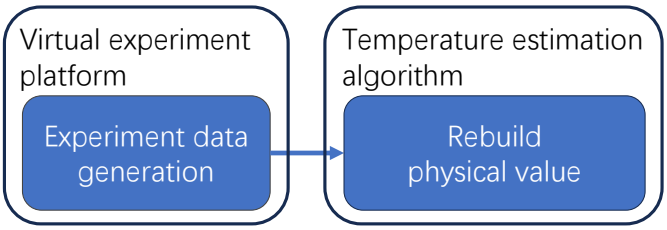

Figure 15: Complete procedure from data generation to model validation

Fig.15 shows the procedure of the application. Firstly, an experiment data set should be generated according to the parameters of the hypothetical material. Then, a temperature estimation algorithm is applied to estimate the temperature of the hypothetical material. Last, a validation procedure is used to check the accuracy and stability of the results of temperature estimation algorithm.

As mentioned in previous sections, these functions is implemented in three programmes. Namely virtual experiment platform, temperature estimation algorithm and validation procedure. Similar to conventional experiment methods, these steps are independent procedures, which means they do not interact with each other.

Accordingly, this chapter will be divided into three sections, which describe the implementation and the parameter settings of the virtual experiment platform, temperature estimation algorithm and validation procedure.

4.1 Experiment data generation

As the first of the three steps mentioned above, it is crucial to generate accurate experimental data correctly. It affects the comparability of the virtual experimental platform with real experiments on the one hand, and the accuracy of the temperature estimation algorithm on the other. As a result, the virtual experimental platform should be able to perform calculations for as many hypothetical materials with different properties as possible.

In order to be able to obtain image similar to image from real camera, the area that the virtual camera is able to capture is set to a 50*50 pixel picture. Fig.16 shows the image obtained from real experiment and virtual experiment platform. The major difference between these two images is the coloring. In real experiment, the raw image was saved as a .tiff file, which obtain the spectral intensity received by the specific channel. Then, the intensity is expressed as brightness of the pixel in the display of the image. This results in the experiment data that is not intuitive and requires specialised software to open these data.

As a result, there are a number of optimisations that have been applied in this virtual

experiment platform. Firstly, the raw digital value of the received spectral intensity was saved in an .xlsx file, which simplifies the reading of the data as well as the conversion. In addition, a .jpg image of each channel similar to the real experiment data is also saved. Different from the real experiment data, colours are used here to indicate the value of the spectral intensity. This improves the readability of the experiment data.

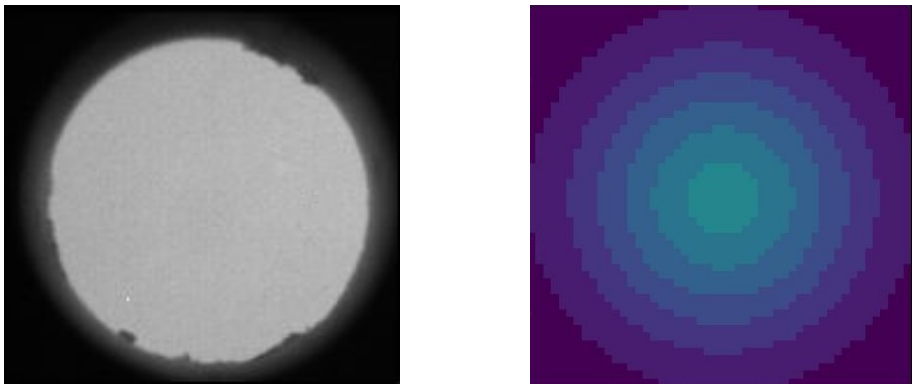

(a) Real experiment data (channel 1) (b) Virtual experiment data (channel 1)

Figure 16: Comparison between real experiment data at $1300K$ (a) and virtual experiment data at $1098K$ (b)

Thus, the observation area is obtained by initialization of the the virtual experiment platform. Temperature field, emissivity model of the hypothetical material and the integration method are the parameters to be defined as the next step.

4.1.1 Temperature field

As mentioned in previous sections, temperature is one of the most important parameters in the virtual experiment platform. In order to obtain results similar to real experiments, a temperature field exists in the observation area. For the purpose of simplifying the calculation process, this temperature field consists of two main regions, a background region at the edge of the observation area, where the temperature is uniformly set to 1000K, and an internal high temperature region, where the temperature follows a predefined distribution.

Fig.17 shows three different temperature distribution which are able to be generated by the virtual experiment platform. Namely linear distribution, gaussian distribution and sigmoid distribution. In order to simplify the visualization process, all temperature fields are generated based on the center point of the observation area. As the temperature of each point is calculated based on the normalized distance d_{rel} or absolute distance d_{abs} to the center point of the observation area.

Linear distribution means that the temperature increases linearly from the back ground area to the center point of the observation area. The details can be found in Eq.4.1. This distribution has the potential to demonstrate the spectral radiation behavior of the hypothetical material in different temperature.

$$t = t_{center} + (t_{background} - t_{center}) \cdot d_{rel} \tag{4.1}$$

Gaussian distribution is also called normal distribution. In this distribution type, the temperature field in observation area obeys gaussian distribution described in Eq.4.2. With the temperature of the center point in observation area equals the defined center

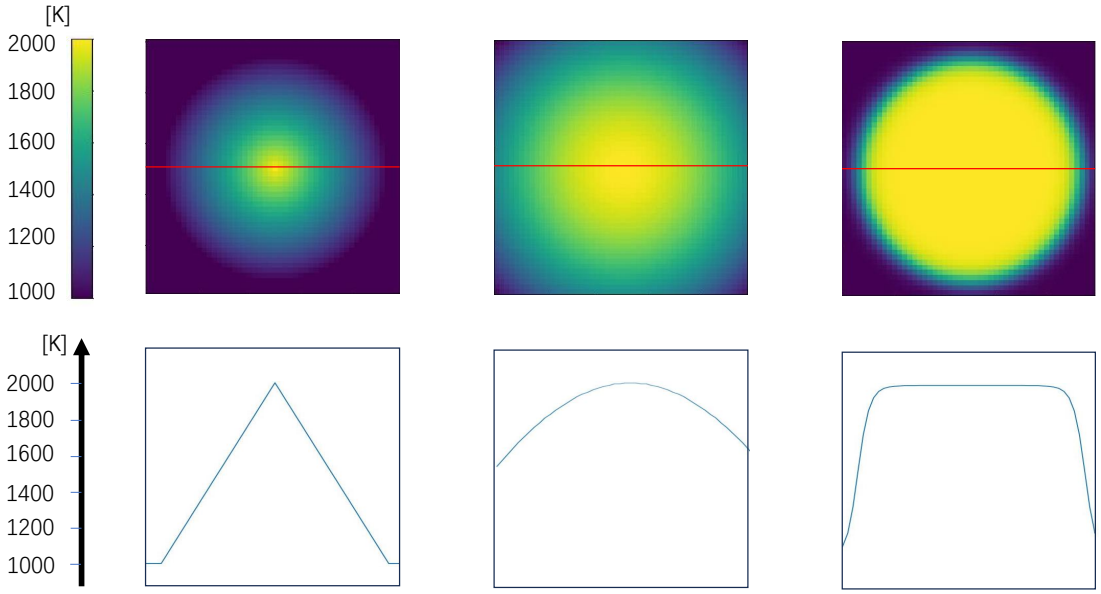

(a) Linear (b) Gaussian (c) Sigmoid

Figure 17: Temperature field of 3 different temperature distribution and the temperature profile in the middle line of the observation area. (a): Linear distribution. (b): Gaussian distribution. (c): sigmoid distribution

temperature. Due to energy input of the system and heat transfer in metal powder, this temperature distribution is more likely to simulate the real situation in experiment.

$$t = t_{center} + (t_{background} - t_{center}) \cdot \exp\left(-\frac{d_{abs}}{2 \cdot \sigma^2}\right) \tag{4.2}$$

Different to the temperature field mentioned before, the temperature in the center region of observation area remains constant. The mathematical expression can be found in Eq.4.3:

$$t = t_{center} + (t_{background} - t_{center}) \cdot \text{sigmoid}\left(\left(\frac{d_{abs}^2}{r_{set}^2} + 1\right) \cdot 1000\right) \tag{4.3}$$

With sigmoid function can be found in Eq.4.4:

$$\text{sigmoid}(x) = \left(1 + \exp\left(-\frac{x}{100}\right)\right) \tag{4.4}$$

Sigmoid function gaves the opportunity to perform the temperature estimation algorithm in a stable temperature. Thus, the potential to investigate the consistency of the temperature estimation algorithm and performance of the noise cancellation program is given.

4.1.2 Emissivity model

Obtaining temperature field of the hypothetical material, an emissivity model is required to calculate the physical value of spectral radiation intensity emitted from the hypothetical material.

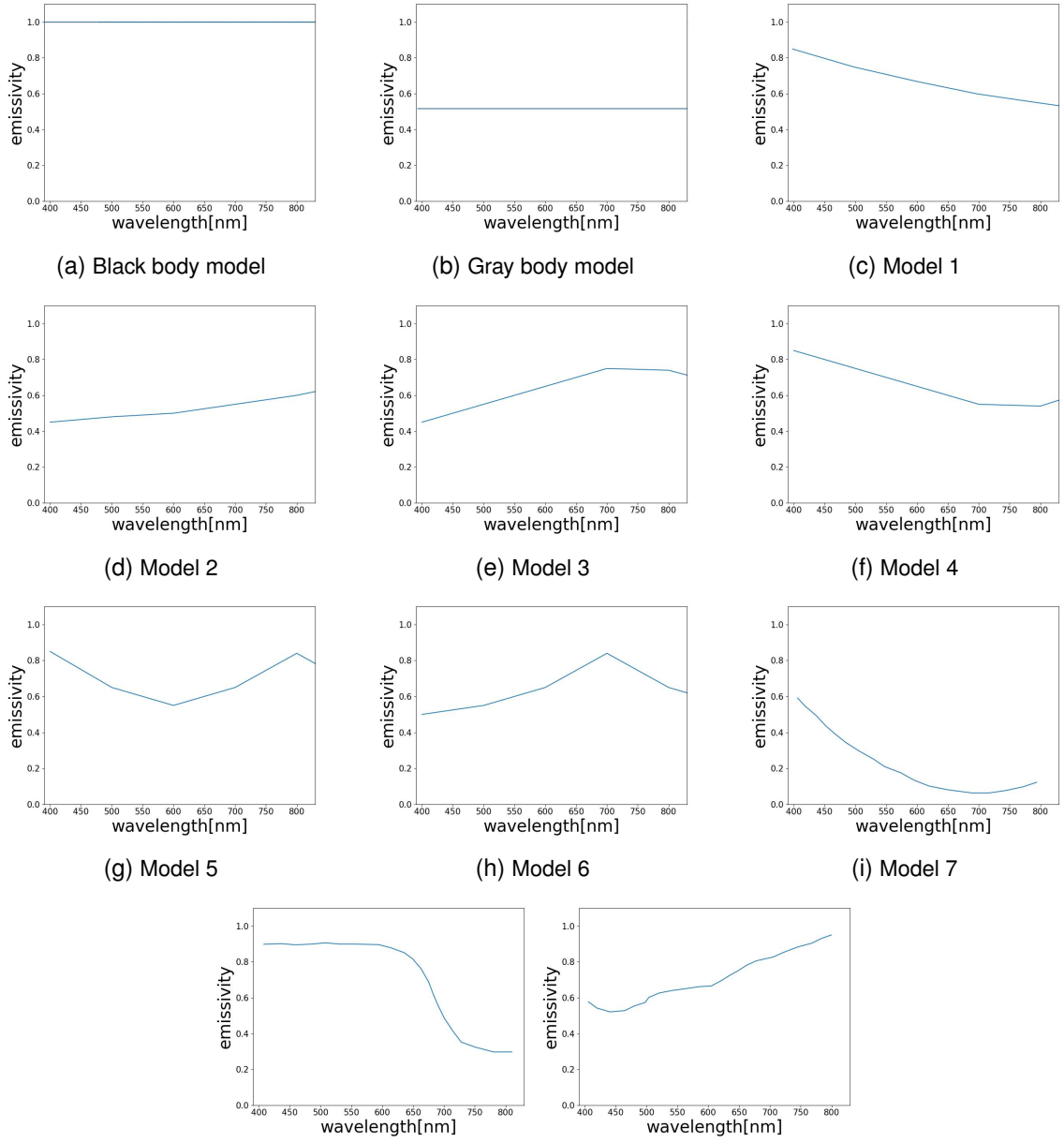

Figure 18: Raw emissivity data used in virtual experiment platform. (a), (b) are black body and gray body; (c) - (h) are hypothetical materials[49]; (i) - (k) are real materials[48].

Since the emissivity of metal powder is wavelength (λ) and temperature (T) relevant, the emissivity model in this virtual experiment platform is formed based on the Eq.4.5.

$$\varepsilon(\lambda, T) = \varepsilon_{raw}(\lambda) \cdot K_T(T) \tag{4.5}$$

The raw emissivity data $\varepsilon_{raw}(\lambda)$ in Fig.18 are obtained by Wang et al.[49] and Taunay et al.[48]. These data sets could be used to simulate the radiation behavior of various hypothetical materials.

Black body and gray body

Fig.18a and Fig.18b represent black body radiation and gray body radiation, respectively. In these two models, emissivity remains constant with respect to temperature and wavelength variations. Consequently, this represents the simplest emissivity model.

Hypothetical material

Model 1 to 6 describe the emissivity of different hypothetical materials based on the emissivity model made by Wang et al.[49]. Model 1 represents the case of monotonically decreasing emissivity, which is also consistent with the emissivity model of iron in solid phase. This model could be used as a simplification of emissivity model of real iron. Model 2 describes a situation where emissivity increases with wavelength. Unlike the material based on model 1, in this case, the emissivity increases with increasing wavelength, and this increase is non-linear. Thus, the non-linear nature of emissivity is represented. Models 3 and 4 represent emissivity as a convex and concave curve. Model 5 depicts a situation where emissivity exhibits two inflection points as wavelength increases. Lastly, Model 6 illustrates a scenario where emissivity shows a single inflection point as wavelength increases. One of the advantages of using a virtual experiment platform is the ability to test a greater diversity of hypothetical materials than what may be feasible in real experiments.

Therefore, it is essential to incorporate certain hypothetical materials that do not exist in reality within the virtual experimental platform. By doing so, it becomes possible to assess the consistency of temperature estimation algorithms under various extreme scenarios, thereby determining the operational limits at which the system can function reliably.

After obtaining the raw data of hypothetical material on the relationship between emissivity and wavelength, the dependence of emissivity on temperature is characterised as a temperature factor $K_T(T)$ in Eq.4.6.

$$K_T(T) = \begin{cases} 1 - T_{ref} \cdot 0.2 & T < T_{melt} \\ \left(1 - T_{ref} \cdot 0.2\right) \cdot 0.1 & T \geq T_{melt} \end{cases} \tag{4.6}$$

With

$$T_{ref} = \frac{T - T_{lb}}{T_{ub} - T_{lb}} \tag{4.7}$$

This temperature factor describes the tendency of emissivity to decrease with increasing temperature between T_{lb} and T_{ub}, on the other hand, it also describes the change of emissivity due to the phase change of the hypothetical material that occurs at melting temperature T_{melt}.

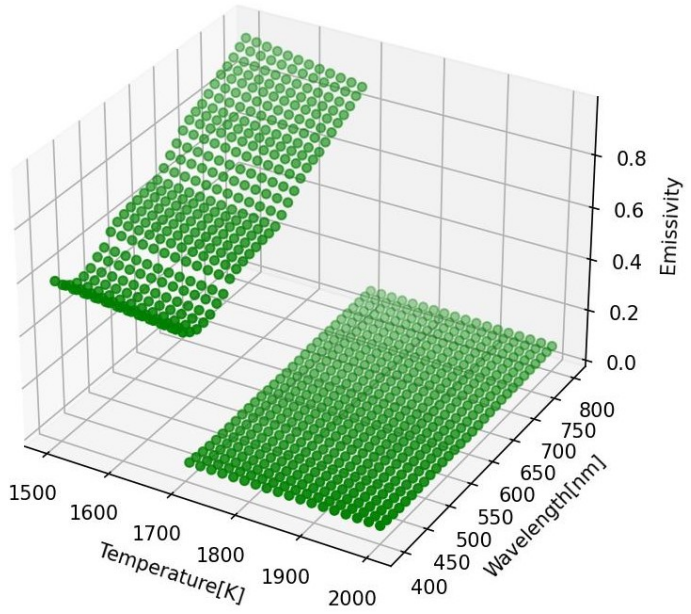

Figure 19: Emissivity value along wavelength and temperature calculated from model 9

Fig.19 shows the emissivity model based on model 9 in different temperature and wavelength. It can be found that the emissivity at a temperature below melting temperature ($1700K$) varies significantly with wavelength. This is caused due to the raw emissivity data. Then, at liquid phase of the hypothetical material, emissivity decreases to a value lower than 0.1.

Thus, the phase change phenomenon of hypothetical material is also characterized, which gives the virtual experiment platform more potential to simulate real experiments.

Real emissivity data from iron

After obtaining the emissivity model for the hypothetical materials, it is necessary to validate the virtual experimental platform using real material data. Therefore, for this study, emissivity data for pure iron obtained by Kobatake et al. and Wantanabe et al. in their experiments were selected for validation [45], [46]. However, these emissivity data do not fully cover the temperature range of 1000 to 2000K and the wavelength range of 400 to 1000nm. To address this limitation and extend the data range in this work, the following approach was adopted:

- The melt point of iron is set to 1811K
- The temperature range of virtual experiment is set as 1500-1900K
- The raw emissivity data can be observed in Fig.20
- The emissivity is calculated as Eq.4.8

$$\varepsilon(T,\lambda) = \begin{cases} \varepsilon_{solid\_raw}(\lambda) \cdot K_T(T) & T < T_{melt} \\ \varepsilon_{liquid\_raw}(\lambda) \cdot K_T(T) & T \geq T_{melt} \end{cases} \tag{4.8}$$

With the normalized temperature factor $K_T(T)$ calculated based on Fig.20b.

$$K_T(T) = \frac{\varepsilon_{raw}(T)}{\varepsilon_{raw}(T_{melt})} \tag{4.9}$$

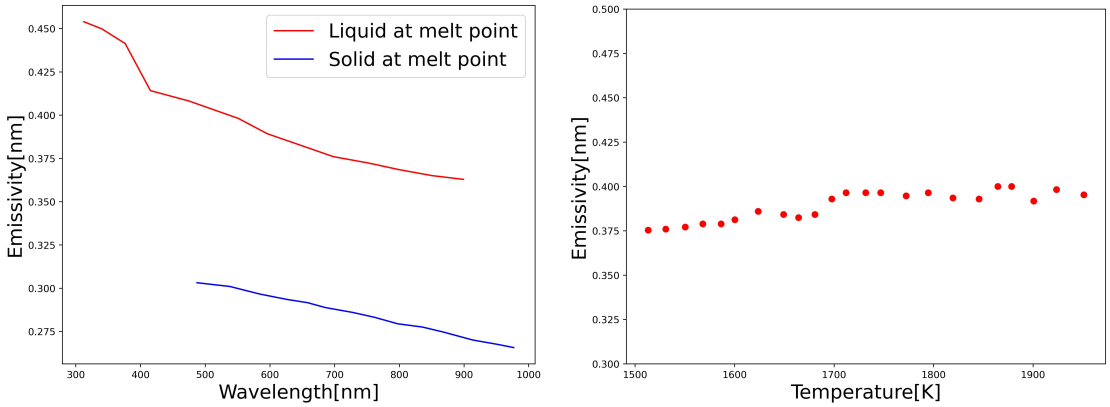

(a) Emissivity $\varepsilon_{raw}(\lambda)$ of liquid iron and solid iron[46] (b) Emissivity $\varepsilon_{raw}(T)$ of iron at 807 nm[45]

Figure 20: Real emissivity data of iron

In contrast to hypothetical materials, the emissivity of real iron is influenced by various factors, such as impurity content, surface roughness, and the content of iron oxide. However, these factors are not within the scope of discussion in this work.

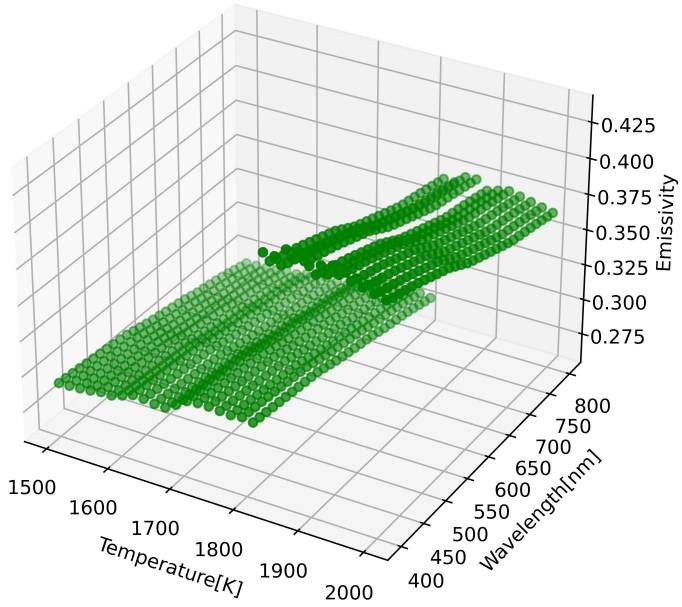

Figure 21: Emissivity value along wavelength and temperature of iron[45], [46]

Fig.21 illustrates the calculated emissivity for pure iron with respect to wavelength and temperature. It can be observed that the emissivity of real materials shows a relatively small variation with changing wavelengths. Consequently, introducing emissivity data from real materials for verification is deemed necessary.

4.1.3 Camera model

After obtaining the temperature field and emissivity model of hypothetical material, the physical value of spectral radiation intensity should be calculated, then, the physical value

of spectral radiation intensity is converted to digital value using camera model, which is the output of the complete virtual experiment platform.

To ensure consistency and scalability within the program for future feature additions, all calculations in the program are conducted using metric units. For instance, temperature is measured in Kelvin, and wavelength is measured in meters. Therefore, it is crucial to note that the unit of wavelength in the camera model's calculations is meters, not nanometers. This ensures dimensional correctness throughout the integration process.

As mentioned in Fig.12, the camera model is based on an integration method, which integrate the spectral intensity received by the sensor along the specific range of wavelength. However, due to the varying quantum efficiency of each channel in sensor, it means that for a virtual camera with 8 channels, each pixel requires 8 independent integration operations. This operation requires a large computational effort. So, in order to accelerate the generation speed and thus reduce the time cost of virtual experiment platform, a parallel computing strategy is introduced.

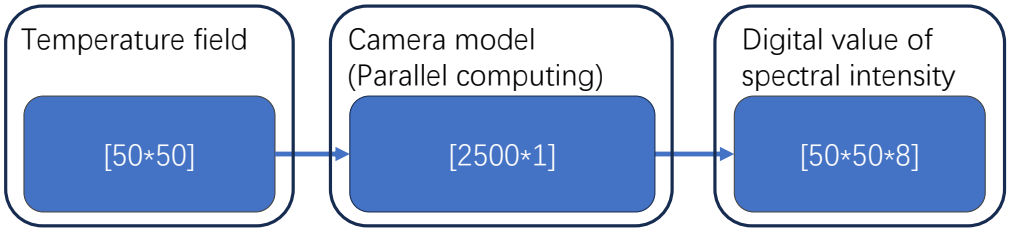

Figure 22: Shape of array used in camera model

The essence of parallel computing lies in decomposing a complex task into multiple tasks and utilizing multithreading techniques to execute these computational tasks simultaneously on different cores of the CPU. In this context, the camera model treats the integral computation on each pixel as an individual task, thereby significantly improving CPU utilization and substantially reducing computational time[52]. To facilitate task partitioning, the dimension of the temperature field mentioned earlier in this section needs to be reduced, from a 50×50 matrix to a one-dimensional array of size 2500×1. This allows for obtaining 2500 parallel tasks. Once the calculations are completed, the resulting matrix of size 2500×8 is then transformed back into a three-dimensional matrix of size $50 \times 50 \times 8$. In this manner, a digital value similar to the data obtained in real experiments is computed.

4.2 Temperature estimation algorithm

After obtaining the digital value of spectral radiation intensity, the tasks of this virtual experiment platform are considered complete, and the next step involves data processing and calculations. The core of the temperature estimation algorithm lies in reconstructing the physical value of spectral radiation intensity based on the known digital values and the choosen parameters. Subsequently, through the implementation of a curve fitting algorithm, the estimated emissivity and temperature can be calculated.

4.2.1 Rebuild physical value of spectral radiation intensity

Hence, it is evident that the process of reconstructing the physical value holds significant importance in the temperature estimation algorithm. This reconstruction process represents the conversion of spectal radiation intensity from its physical value to a digital value. By analyzing the reconstructed results, the relationship between the physical value (I_{rec}) and the parameters (T, k) to be fitted can be established, where T and k are derived from Eq.3.7. Subsequently, by performing curve fit algorithm between the reconstructed physical value and the experimental data, we can obtain the parameters (T, k) that best fit the real data. Therefore, it becomes apparent that the reconstruction of the physical value can affect the accuracy of the temperature prediction algorithm discussed in this thesis.

As mentioned in Eq.3.7, the reconstructed physical value of spectral radiation intensity is generated based on the integration method. It can be observed that the digital value can be considered as a function of temperature of hypothetical material T and parameters of emissivity model k.

$$I^i_{rec}(k,T) = q \int B(\lambda,T) \cdot \varepsilon(\lambda,k,T) \cdot \eta^i_{camera} d\lambda \tag{4.10}$$

Eq.4.10 shows the mathematical expression of reconstructed physical value of spectral radiation intensity of i_{th} channel. So, the current objective is to minimize the cost in Eq.3.8 by optimizing the values of k and T. In other words, the goal is to make the reconstructed spectral radiation intensity $I_{rec}(k,T)$ as close as possible to the values obtained in virtual experiments. By minimizing the cost function, the temperature estimation algorithm aims to achieve a high level of accuracy and fidelity in calculating the temperature based on the reconstructed digital values.

4.2.2 Emissivity model used for calculation

In the previous section, it is evident that the temperature estimation algorithm is essentially performing a curve fit algorithm on the parameters of the emissivity model and temperature of the hypothetical material. Therefore, the choice of the emissivity model significantly impacts the accuracy of the temperature estimation algorithm. In order to enhance the generality of this temperature prediction algorithm and prevent overfitting, a hypothesis is proposed: the temperature prediction algorithm is unaware of the material's emissivity characteristics. Hence, it is necessary to use a different emissivity model from the one used in the virtual experiment platform to reconstruct the digital value of spectral radiation intensity.

Based on mentioned above, the temperature estimation algorithm introduced in this paper tested several different emissivity models, namely:

1. Linear model
2. Linear square model
3. Quadratic model
4. Exponential model
5. A combined model composed of the linear square and exponential models

These models are distinguished based on the relationship between emissivity and wavelength. Each model represents a different mathematical expression that describes how emissivity varies with wavelength. In order to simplify the calculation process and thus set boundary conditions of parameters k in emissivity model, all wavelength used in this emissivity model is normalized wavelength λ_{norm}. The mathematical expression can be described as followed:

$$\lambda_{norm} = \frac{\lambda - \lambda_{lb}}{\lambda_{ub} - \lambda_{lb}} \tag{4.11}$$

To enhance the readability of the formula, the parameter k in Eq.4.10 is written in vector form in Eq.4.12 based on the number of parameters in emissivity model.

$$k = \begin{pmatrix} a \\ b \\ c \end{pmatrix} or \begin{pmatrix} a \\ b \end{pmatrix} \tag{4.12}$$

With the lower boundary of wavelength $\lambda_{lb} = 500nm$ and the upper boundary of wavelength $\lambda_{ub} = 1000nm$. Thus, the input of the emissivity model used in temperature estimation algorithm is thus dimensionless number.

Linear model

Linear model refers to a linear relationship between emissivity and wavelength, which could be written as Eq.4.13:

$$\varepsilon(\lambda) = a \cdot \lambda_{norm} + b \tag{4.13}$$

The linear model represents the simplest and most straightforward emissivity model. It provides an easy way to visualize the calculated emissivity model and reduces complexity in defining various boundary conditions within the emissivity model.

Linear square model

The linear square model is distinct from the linear model, as it incorporates three parameters representing the coefficients of the quadratic term, the linear term, and the constant term. Its mathematical expression can be described as Eq.4.14:

$$\varepsilon(\lambda) = a \cdot \lambda_{norm}^2 + b \cdot \lambda_{norm} + c \tag{4.14}$$

The linear square model can be used to describe more intricate emissivity models for materials. With an additional parameter compared to the previous linear model, it offers increased degrees of freedom for curve fitting, enabling a better fit to complex shapes. Nevertheless, the augmented complexity may also lead to a higher risk of overfitting as well as increase of computational demand required.

Quadratic model

Consequently, in order to simplify the computation of the linear square model, the quadratic model was introduced. In this model, the coefficient of the linear term in the original linear square model is set to 0. This simplification leads to a reduction in the number of parameters within the emissivity model. The emissivity model can be expressed as Eq.4.15

$$\varepsilon(\lambda) = a \cdot \lambda_{norm}^2 + b \tag{4.15}$$

Exponential model

In the exponential model, emissivity is exponentially related to wavelength. Due to the monotonic nature of the exponential function, this model enhances the accuracy of parameter estimation along the gradient descent of the cost function during curve fitting, thereby improving the computational efficiency. The mathematical expression can be expressed in Eq.4.16:

$$\varepsilon(\lambda) = \exp(-a \cdot \lambda_{norm} - b) \tag{4.16}$$

For materrials commonly used in PBF-LB/M, emissivity tends to decrease with increasing wavelength. Therefore, to reduce the range of parameters during curve fitting, the exponent term $a \cdot \lambda_{norm} + b$ was set as non-negative value.

Mixed model

This model is a combination of two models. In Fig.19, it can be observed that the emissivity of the virtual material undergoes significant changes when the temperature exceeds the material's melting point, and the emissivity variations become smaller in the liquid phase. Therefore, when emissivity changes are relatively small, i.e., when the material is in the liquid phase, the exponential model is more suitable. On the other hand, when emissivity changes are more pronounced, i.e., when the material is in the solid phase, the linear square model is more appropriate. This approach not only improves the computational accuracy of the model in the solid region but also ensures the computational efficiency of the model in the liquid region.

$$\varepsilon(\lambda) = \begin{cases} \varepsilon(\lambda)_{solid} & T \leq T_{melt} \\ \varepsilon(\lambda)_{liquid} & T > T_{melt} \end{cases} \tag{4.17}$$

In this model, the computation starts with the linear square model. The computed results are then filtered to identify points where the temperature exceeds the material's melting point. Subsequently, the exponential model is utilized to recompute the emissivity and temperature for those specific points. Finally, the results from both calculations are combined to obtain a higher precision outcome. However, this process demands higher computational resources. Consequently, it is observed that this model significantly increases the computational time required for temperature estimation algorithms.

4.2.3 Curve fit algorithm

After obtaining the reconstructed physical values of intensity, a curve fit algorithm is required to determine temperature and the parameters of the emissivity model that best align with the actual received intensity. However, in this work, both the data obtained from the virtual experimental platform and the data from real experiments are not continuous spectral intensities. Conversely, the input for this temperature estimation algorithm is a two-dimensional array with dimensions of 8x2, which can be regarded as 8 samples of a continuous physical value.

Fig.23 illustrates the reconstructed physical value for each channel and the corresponding physical values from the original experimental data. It is evident that this approach

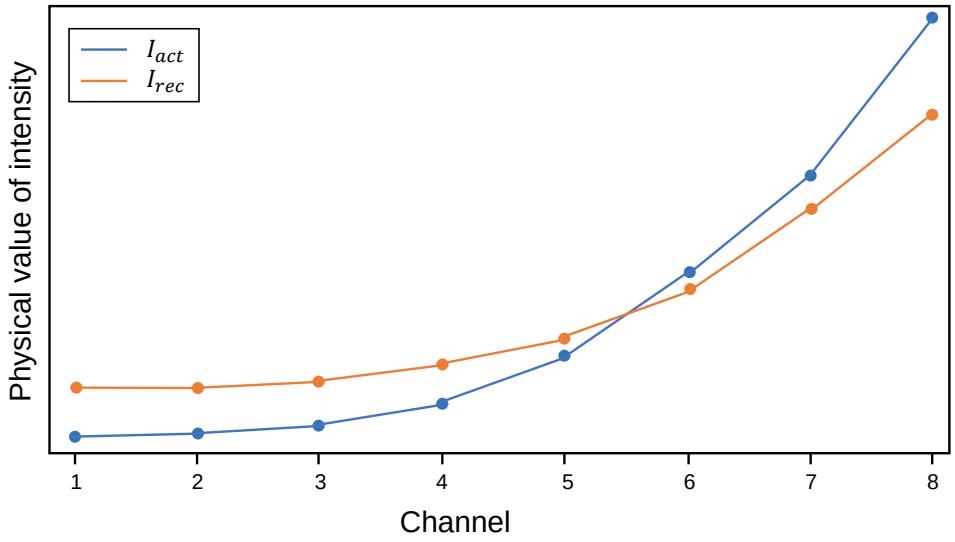

Figure 23: Comparison between actual received intensity I_{act} and reconstructed intensity I_{rec} of one point

simplifies the visualization of independent channel data and facilitates the utilization of this profile for curve fitting purposes.

4.2.4 Parameters in temperature estimation algorithm

The temperature estimation algorithm uses numerous parameters, which significantly impact the precision and consistency of the computed results. Therefore, it is essential to set boundary conditions for these parameters.

Wavelength range

In Fig.11, it can be observed that the total quantum efficiency of the sensor η_{camera} decreases to 0 when the radiation wavelength exceeds 900 nanometers. This effect is attributed to the presence of a filter on the sensor. Consequently, when reconstructing the physical values of the spectral radiation intensity, the integration limits are set to be within the range of 500 nanometers to 1000 nanometers. This approach ensures that the essential information is captured while reducing the computational resources required for integration and thus improving the computational speed.

Boundary condition of estimated temperature

In the temperature estimation algorithm, the process starts with an initial guess, which is used to perform the first reconstruction of the physical values of the spectral radiation intensity. This reconstruction yields a cost function and a gradient that minimizes the cost function. The algorithm then adjusts the parameters to be optimized along this gradient before proceeding to the next iteration. It is evident that the choice of the initial guess significantly influences the computational efficiency of the program and can help avoid potential physically meaningless local minima.

To address this, it is mandated that the predicted temperature in the temperature estimation algorithm lie within the range of 500 to 2000K. This constraint ensures that the algorithm operates within a physically meaningful and relevant temperature range, preventing

unrealistic results and potentially leading to a more effective and efficient optimization process.

Boundary condition of estimated emissivity

Unlike the boundary conditions applied to the estimated temperature, the boundaries for emissivity are much narrower. This is due to the physical definition of emissivity mentioned earlier in the text. Therefore, it is necessary to apply a boundary condition of $0 < \varepsilon < 1$ for emissivity during the calculations. However, in the curve fit algorithm mentioned in this work, emissivity is not a variable to be determined. Hence, it becomes necessary to incorporate this boundary condition directly into the emissivity model.

5 Calcualtion results and analysis

Once all the experiment data and parameters are determined, the results of the calculation should be presented and analyzed. Thus, the accuracy, consistency, pros and cons of the virtual experiment platform and temperature estimation algorithm can be systematically analyzed.

5.1 Calculation results

In virtual experiment platform and temperature estimation algorithms, emissivity is considered as a function of radiation wavelength and temperature. Consequently, it varies with changes in temperature and radiation wavelength. This variability is advantageous for enhancing algorithm precision but introduces difficulties in visualizing computation results. Furthermore, temperature estimation algorithm doesn't directly calculate the emissivity of materials; instead, the algorithm optimize the parameters k of the emissivity model. Thus, the emissivity data of each point is a function of wavelength λ and thus cannot be directly visualized. To address this, a simplified approach for visualizing emissivity is introduced, which allows for a more intuitive representation of emissivity without compromising the accuracy of the computational process.

$$\varepsilon_{sim} = \overline{\varepsilon(\lambda)} \tag{5.1}$$

Eq.5.1 presents the mathematical expression for this simplification. ε_{sim} represents the simplified emissivity value, and $\varepsilon(\lambda)$ denotes the emissivity model's value at wavelength λ. In other words, in this work, the visualization of emissivity is derived from the average value of emissivity model data within the wavelength range of 500 to 1000 nanometers.

By employing the same simplification method in the generation of experimental data and subsequent temperature estimation algorithm, the validity of the program's verification is ensured. This consistency guarantees that the comparison between the data used for validation remains effective and reliable throughout the process.

After obtaining a standardized emissivity visualization method, it is necessary to validate the calculation results. For the convenience of validation, several data that cannot be obtained in real experiments, such as temperature and emissivity of hypothetical material have been saved in several files in the virtual experiment platform and used to check the accuracy in validation process.

5.1.1 Raw experiment data from virtual experiment platform

In order to assess the performance of the temperature estimation algorithm at different temperatures and facilitate visual analysis, a linear temperature distribution is employed during the validation process. The background temperature is set to 1000K, while the center point's temperature is set at 1900K. Details is shown in Fig.24. Simultaneously, the melting point of the hypothetical material is defined as 1600K (except black body and gray body hypothetical material). This approach allows for the comparison of data obtained from the virtual experimental platform with that from real experiments, while checking

the accuracy of the temperature estimation algorithm in both solid and liquid phase of the hypothetical material.

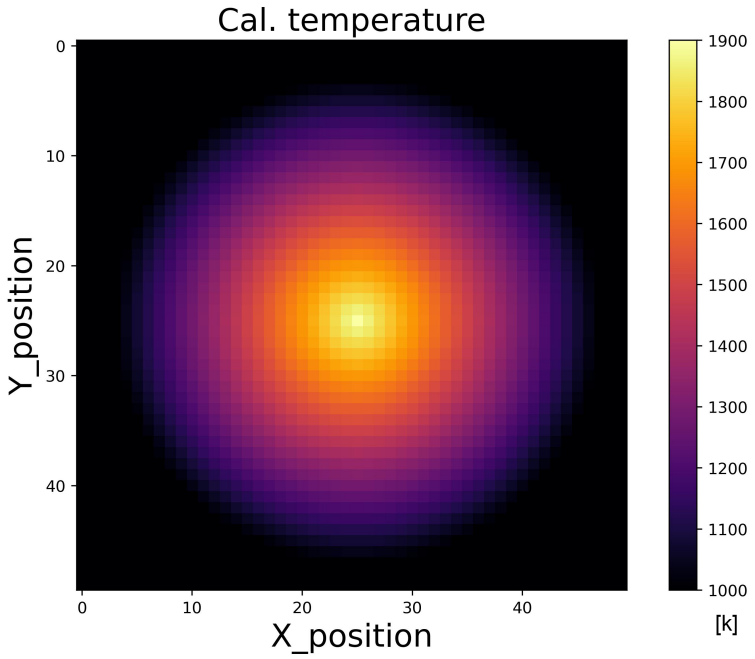

Figure 24: Temperature field used in validation

After obtaining a temperature field, the virtual experimental platform used the aforementioned 12 different emissivity models to generate 12 different sets of experimental data. This approach simulated the radiative behavior of 12 hypothetical materials under identical temperature conditions in the virtual experiment platform.

As a result, Fig.25 displays the emissivity fields generated by defferent model along with their corresponding radiation intensities. To conserve space, digital values of channel 4 in each experiment data were chosen as representatives of the intensity data.

It can be observed that in blackbody and gray body materials, emissivity is not dependent on the material's temperature or status. As a result, the emissivity field exhibits a uniform color distribution. This characteristic also leads to a situation in the calculation of radiation intensity, where the physical values received by the virtual camera show a maximum at the center point and decrease as the temperature decreases.

However, in more general material models, such as Model 1 and Model 8, emissivity undergoes a discontinuity when the material transitions from the solid state to the liquid state. This is due to the fact that the emissivity of liquid phase is smaller than that of solid phase. Consequently, the radiation intensity received by the virtual camera decreases at the boundary when the material changes from solid to a liquid. Subsequently, at the center point, the radiation intensity emitted by the hypothetical material increases again due to the rise in temperature. This phenomenon results in a bright halo appearing in the digital value of channel 4 in the images. The center of this halo exhibits a point with higher brightness level.

Indeed, the non-uniform intensity distribution caused by different emissivity characteristics of materials can lead to challenges for the subsequent temperature estimation algorithm. The intensity distribution along wavelength differs due to the different emissivity model of the hypothetical material. Consequently, in the curve fit algorithm, the most suitable

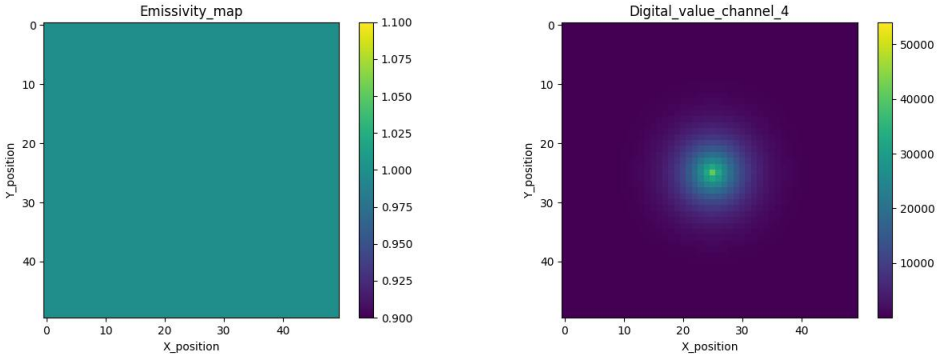

(a) Black body

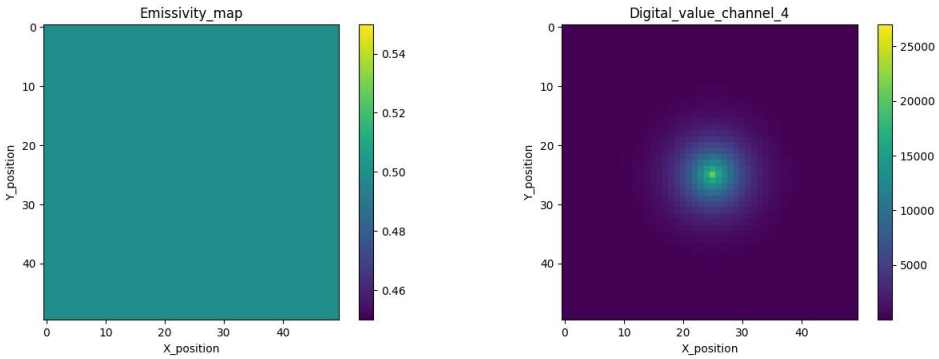

(b) Gray body

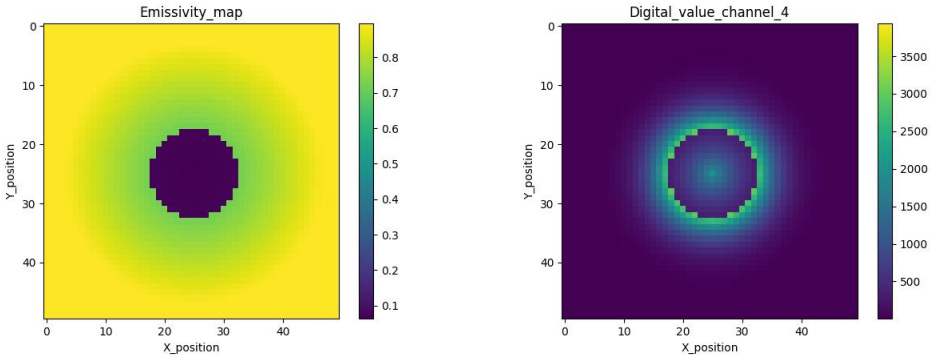

(c) Model 1

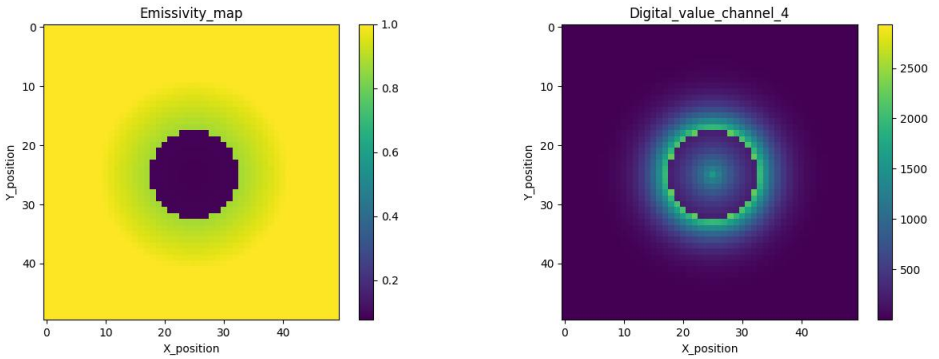

(d) Model 8

Figure 25: Emissivity field and digital value of radiation intensity in channel 4 for black body material(a), gray body material(b), material based on model 1(c) and model 8(d)

emissivity model for the current material may change accordingly. Therefore, particular attention should be given to the phase transition of the hypothetical material in the context of temperature estimation.

After investigating the impact of different emissivity models on material radiative characteristics, it is necessary to explore the relationship between digital values of radiation intenstiy across different channels. Fig.26 displays the images of a material based on Model 1 at a temperature of 1900K, captured using 8 different channels. In this image, it can be observed that the intensity received by the virtual camera increases with the channel number.

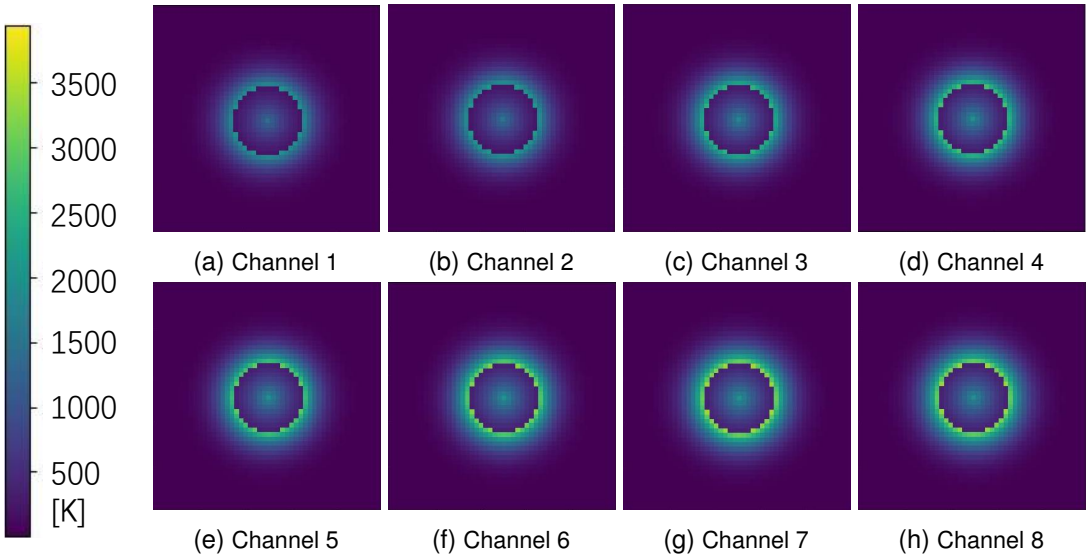

Figure 26: Digital value of each channel by hypothetical material based on model 1 and a linear temperature distribution with center temperature 1900K

According to Wien's displacement law introduced in previous chapter, as described in Eq.3.3, when the hypothetical material's temperature is 1900K, it is easy to calculate the peak wavelength (λ_{peak}) as 1525nm. Consequently, it can be inferred that the spectral intensity of blackbody radiation emitted by the hypothetical material will increase with increasing wavelength across the entire observation range ($500-1000nm$). This characteristic aligns with the real experimental observation, where the spectral radiation intensity received by a camera increases with the channel number.

5.1.2 Estimated temperature field and emissivity field

After obtaining reliable experimental data, it is essential to perform temperature estimation algorithm to validate the accuracy of the temperature estimation algorithm. The temperature estimation algorithm will yield two primary results: the estimated temperature field and the simplified estimated emissivity field. These computational results will be presented:

1. Estimated temperature field: The estimated temperature field represents the spatial distribution of temperature across the observation area. This is a most important output of the whole temperature estimation algorithm.

2. Simplified estimated emissivity field: The simplified estimated emissivity field denotes the variation of emissivity across the observation area. It could be used to indentify

the phase change area and thus find the improvement potential.

For visualization, the presentation of the computational results will be categorized based on the emissivity model used in the temperature estimation algorithm. As the experimental data for these temperature estimation algorithm use the same temperature distribution, relative error of temperature is employed here to represent the accuracy of the computations. To save space, the results of calculations for blackbody materials and materials based on Model 1 are selected for presentation.

In real experimental data, due to the limitations of the sensors, it is not possible to simultaneously observe the radiation intensity of the non-laser-heated region and the radiation intensity of the laser-heated region. In the virtual experimental platform, the temperature of the background region is assumed to be uniform, which is comparable to the real situations. Consequently, in order to avoid introducing statistical errors, the calculation results of the temperature estimation algorithm in background region can be considered as negligible.

Linear model

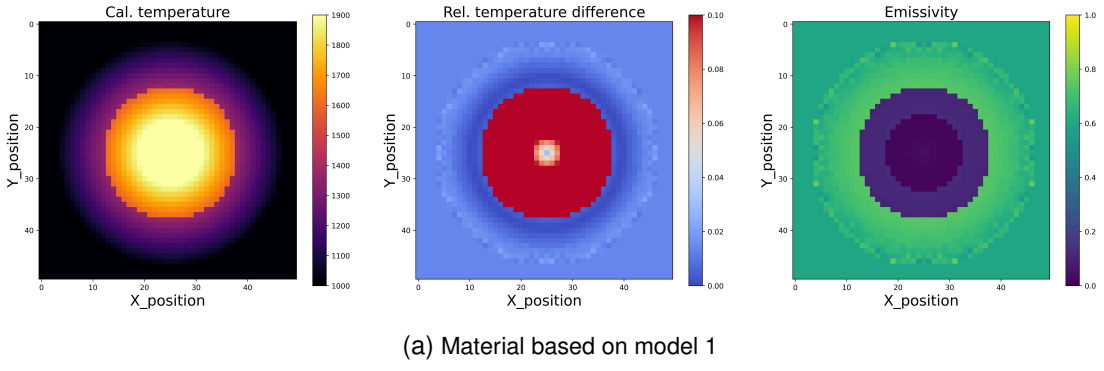

(a) Material based on model 1

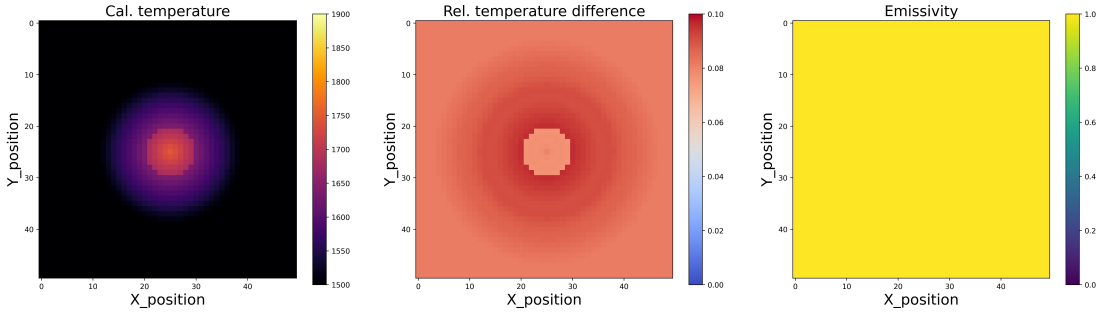

(b) Material based on real iron data

Figure 27: Calculation results of linear model

Fig.27 demonstrate the calculation result on material based on model 1 and real data from iron. It can be found that the calculation result is more stable in real data due to the material character.

It can be observed that relative bias are present in the estimations based on two different materials. Moreover, this relative bias experiences a sudden change with increasing temperature, represented by a red circle in the figure. The reason behind this phenomenon can be considered as follows, at the boundary of the circle, the material undergoes a phase change from solid to liquid, leading to a rapid change in emissivity. The linear model is

only able to simulate linear emissivity models, which fails to adequately fit the variations occurring at this point, resulting in significant deviations in the temperature estimations.

It can be found in table 1 that in the computation of linear models, calculation results based on real data exists relatively low average relative error and the lowest standard deviation. This indicates that the linear model maintains a higher level of consistency when performing calculations on real materials. It also achieves a maximum relative error of no more than 9.6%. However, when performing calculations on other hypothetical materials, the linear model may produce relatively large errors, particularly for model 8, which has a high standard deviation, meaning the low consistency in the calculations. As mentioned in previous sections, this decrease in computational consistency could be attributed to the fact that the emissivity of materials based on model 8 undergoes a sudden change as the wavelength increases, which is a potential reason for the decline in calculation consistency.

Linear square model

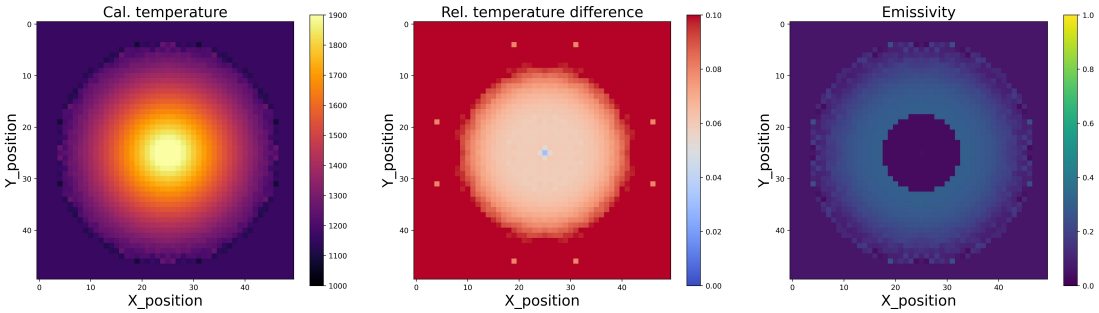

(a) Material based on model 1

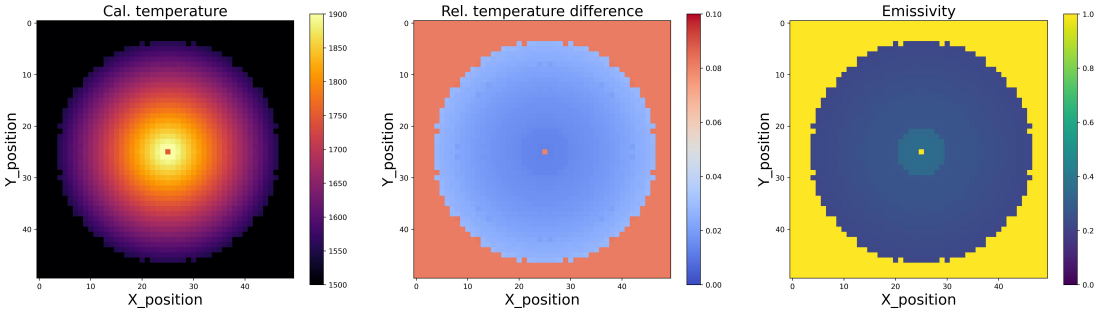

(b) Material based on real iron data

Figure 28: Calculation results of linear square model

Fig.28 presents the computational results of the linear square model for the virtual experimental data based on both model 1 and real iron. It can be observed that the results obtained by the linear square model do not exhibit the ring-like pattern that emerges with increasing temperature for the hypothetical material. This is because the linear square model possesses better capabilities to fit complex emissivity behaviors. In the emissivity plot on the right side, it is evident that the linear square model accurately reproduces the abrupt change in emissivity in the liquid region without causing a significant increase in temperature estimation errors. Thus, it can be concluded that the linear square model outperforms the linear model in terms of temperature estimation accuracy.

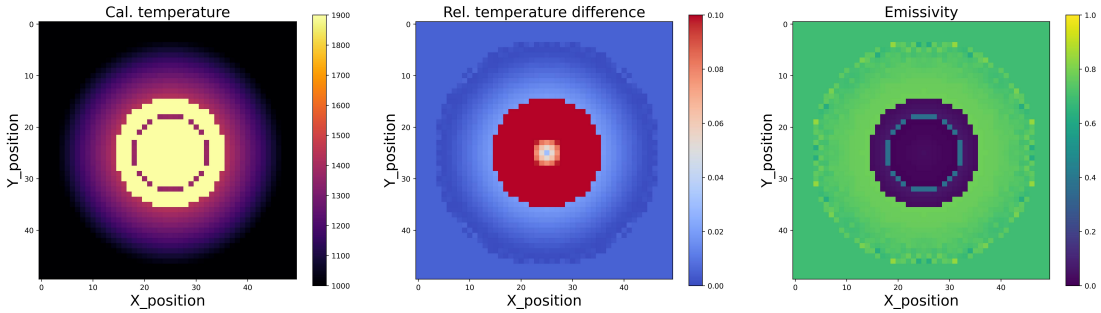

(a) Material based on model 1

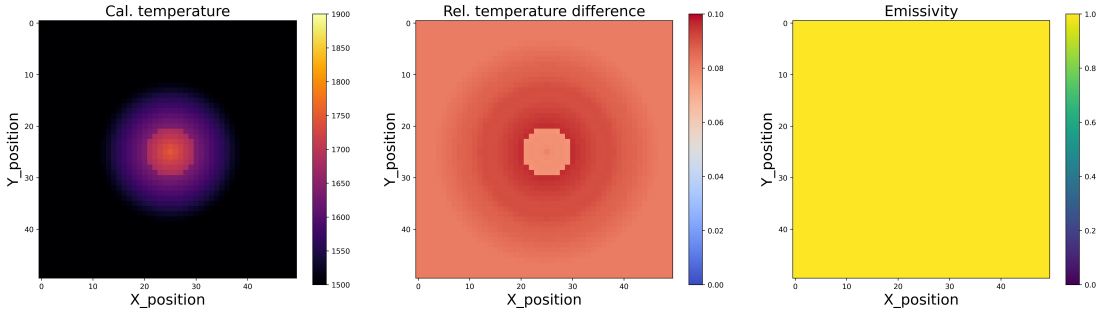

(b) Material based on real iron data

Figure 29: Calculation results of quadratic model

Quadratic model

Unlike the previously mentioned linear square model, the quadratic model has one fewer parameter, resulting in fewer degrees of freedom for the emissivity model. In fact, based on Eq.4.15 from the paper, this mathematical model ss y-axis symmetry. Considering the physical meaning of emissivity, it can only be used to fit emissivity models that are either monotonically increasing or monotonically decreasing.

As a result, as shown in Fig.29, it can be observed that in the computations based on model 1 for the material, the performance of the temperature estimation algorithm is better at the central point (the location with the highest temperature) compared to other regions due to less variations in emissivity. The results of the emissivity field demonstrate that the algorithm accurately identifies the boundary regions between liquid and solid materials.

However, for computations involving real materials, the algorithm struggles to accurately estimate the emissivity of hypothetical materials, leading to errors in temperature calculations. Nevertheless, it is still evident that the temperature estimation algorithm based on the quadratic model performs better on real materials compared to hypothetical materials.

Exponential model

In the exponential model, the emissivity model follows the form of an exponential function. The two parameters in the emissivity model allow for translation and deformation of the exponential function. This enables the temperature estimation algorithm to be applicable to a wider range of materials with different emissivity characteristics. Fig.30 presents the results of this temperature estimation algorithm for materials based on model 1 and real iron.

Due to the physical meaning of emissivity, the value of emissivity is defined within the range

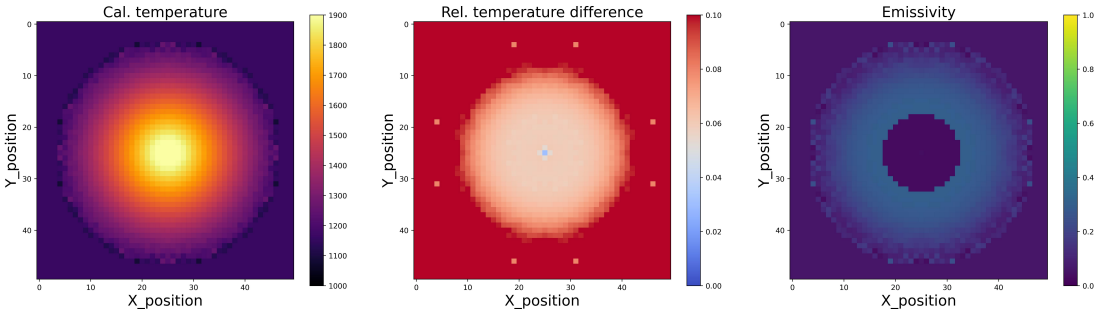

(a) Material based on model 1

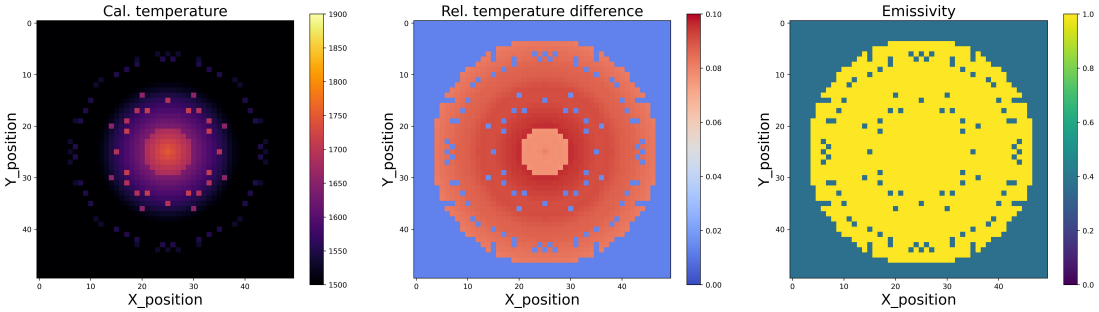

(b) Material based on real iron data

Figure 30: Calculation results of exponential model

of 0 to 1. Thus, constraints must be imposed on the emissivity model. Thus, calculated from Eq.4.16, the following constraints can be introduced:

$$-a \cdot \lambda_{norm} - b \leq 0 \tag{5.2}$$

Therefore, the derivative of emissivity with respect to wavelength is obtained as:

$$\frac{d\varepsilon(\lambda)}{d\lambda_{norm}} = -a \cdot e^{-a \cdot \lambda_{norm} - b} \tag{5.3}$$

For each data point, the emissivity computed based on the exponential model is either monotonically increasing or decreasing, depending on the sign of parameter a. This characteristic of the model leads to an increase in computational speed and a decrease in computational accuracy when strong non-monotonic behavior is observed in the emissivity characteristics of the material.

In Fig.30, it is evident that material based on model 1 exhibits an almost linear relationship between emissivity and wavelength in the liquid state. This enables the temperature estimation algorithm to accurately calculate the boundary region between the liquid and solid states and achieve high computational precision within the liquid state region.

However, when applying the temperature estimation algorithm to real iron data, it fails to accurately calculate the emissivity values. This discrepancy is due to the fluctuation observed in the emissivity of real iron as a function of wavelength. The emissivity of iron in the liquid state is closer to the numerically derived values of the algorithm than in the solid state, leading to erroneous conclusions of higher computational accuracy at the central points.

Mixed model

Eq.4.17 indicates that the mixed model is composed of two components: a low-temperature emissivity model and a high-temperature emissivity model. This approach offers a significant advantage as the temperature estimation algorithm can fit to the different emissivity characteristics observed in the liquid and solid regions. But the computational time has significantly increased due to the utilization of two different emissivity models.

$$\varepsilon(\lambda) = \begin{cases} a \cdot \lambda_{norm}^2 + b \cdot \lambda_{norm} + c & T \leq T_{melt} \\ \exp(-a \cdot \lambda_{norm} - b) & T > T_{melt} \end{cases} \tag{5.4}$$

In this work, the low-temperature emissivity model is represented by linear square model, while the high-temperature emissivity model is described using exponential model. This choice is driven by the fact that the emissivity of the hypothetical material exhibits significant fluctuations in the solid-state region, making it more suitable to be computed using linear square model to better capture its behavior. Conversely, in the liquid state region, the emissivity of the hypothetical material exhibits relatively smaller fluctuations, making it possible to use a faster computational exponential model without decreasing the accuracy.

From Fig.31, it is evident that the mixed model accurately identifies the boundaries between the liquid and solid regions for both model 1 based material and real iron-based material. Additionally, it accurately recognizes the regions that require recalculations in the case of blackbody materials. This indicates that the model is applicable to materials with different emissivity characteristics.

Regarding the temperature estimation results, the model demonstrates high precision in calculating temperatures for blackbody materials and materials based on model 1. In these cases, the error in the center region is less than 7%. However, the model shows a region of relatively lower accuracy when applied to real iron-based material. In this region, the emissivity values are erroneously computed as 1, leading to an increase in temperature calculation bias. This discrepancy can be attributed to the use of the exponential model in the temperature estimation algorithm, as mentioned earlier, which introduces errors when calculating the emissivity of real iron in its liquid state.

5.2 Statistical results and analysis

After obtaining all calculation results, some statistical results can be found in tabel 1. To mitigate any negative impact of background regions on the statistical results of the temperature estimation algorithm, only the computation results from the central area of the observation area are considered here. As linear temperature distribution is employed for the hypothetical materials, temperature is used to determine whether the point is within the central area. These conditions can be formulated as follows:

$$P = \begin{cases} P_{center} & T \geq T_{edge} \\ P_{background} & T < T_{edge} \end{cases} \tag{5.5}$$

With $T_{edge} = 1200K$ for materials based on model and $T_{edge} = 1600K$ for materials based on real iron data. This is due to the fact that in the virtual experimental platform, the temperature of the background area in the experiments based on real iron data is set to $1500K$.

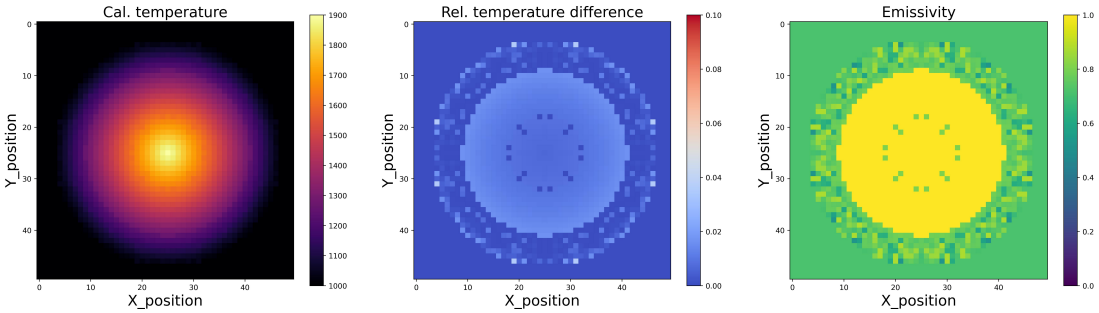

(a) Black body material

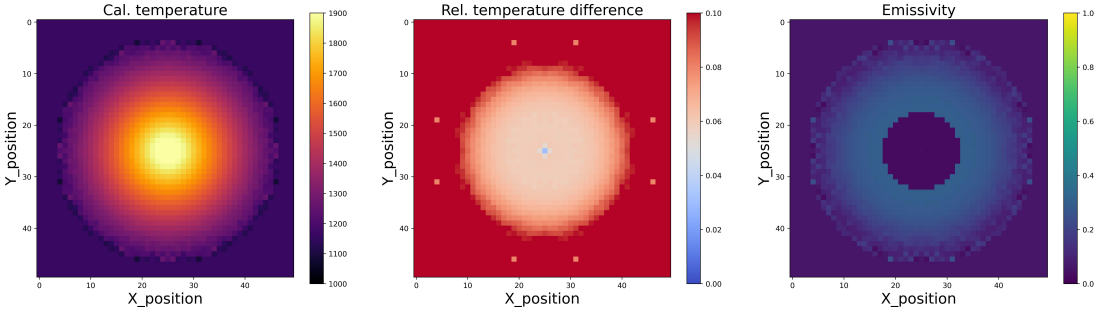

(b) Material based on model 1

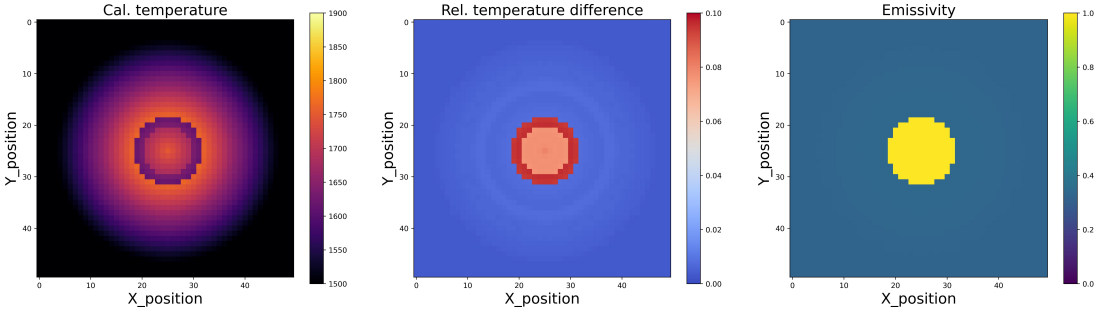

(c) Material based on real iron data

Figure 31: Calculation results of mixed model

Table 1 presents the statistical results of five different temperature estimation algorithms: linear model, linear square model, quadratic model, exponential model and mixed model. These algorithms were applied to blackbody materials, real materials, and materials based on Model 1-9. The statistical metrics calculated for each algorithm include:

1. Mean Difference(Difference)
2. Mean Relative Error(Rel. difference)
3. Standard Deviation(SD)
4. Maximum Relative Error
5. Minimum Relative Error

Mean Difference

The mean difference describes the difference between the calculated temperature T_{cal} and the actual temperature T_{act}. It intuitively demonstrates the accuracy of the temperature estimation algorithm. It is defined by the following equation:

$$E = \overline{T_{cal} - T_{act}} \tag{5.6}$$

Mean Relative Error

The mean relative error describes the relative difference between the calculated temperature T_{cal} and the actual temperature T_{act}. To avoid mutual cancellation between positive and negative deviations, the absolute value of the relative deviation is used here. The mathematical equation can be found as follows:

$$E_{rel} = \overline{\left| \frac{T_{cal} - T_{act}}{T_{act}} \right|} \tag{5.7}$$

Standard Deviation

The standard deviation is used to describe the distribution of differences between the calculated temperature T_{cal} and the actual temperature T_{act}. Since a linear temperature distribution is used, the temperature range of materials within the observed area is relatively large. Hence, this standard deviation can be used to characterize the consistency of the temperature estimation algorithm's results under different temperature conditions. The definition can be found by the following equation:

$$\sigma = \sqrt{\frac{\sum |T_{cal} - T_{act}|^2}{N}} \tag{5.8}$$

With N represents the number of points involved in the statistical analysis.

Min. and Max. Relative Error

These two parameters describe the maximum and minimum values of the relative difference between the calculated temperature T_{cal} and the actual temperature T_{act} over the entire statistical region. These parameters can be used to observe the maximum and minimum

errors caused by the temperature estimation algorithm. This allows for a visual assessment of the effectiveness boundaries of the temperature estimation algorithm's results.

5.2.1 Performance of different temperature estimation algorithms

After obtaining the statistical results of the temperature estimation algorithm, it is necessary to analyze these results. Since the statistical outcomes encompass the calculations of various temperature estimation algorithms for different materials, the analysis consists of two main parts: one involves the performance analysis of different temperature estimation algorithms, while the other concerns the performance analysis of the temperature estimation algorithm for different materials.

In Table 1, it can be observed that each temperature estimation algorithm produces different results for the same material.

When applied to blackbody materials, all algorithms achieve accuracy within 5% error. However, it is evident that the linear square model exhibits lower precision compared to other models, and simultaneously, the standard deviation of its calculations is significantly higher than that of other temperature estimation algorithms. This discrepancy could be attributed to the linear square model having an additional parameter, which makes the curve-fitting process more prone to encountering local minima and prematurely terminating the computation.

Indeed, in addition to linear square model's performance on blackbody materials, the temperature estimation algorithm based on the linear square model consistently achieves lower relative errors and standard deviations compared to other temperature estimation algorithms when applied to different materials. This indicates that the linear square model not only attains higher accuracy but also exhibits a higher level of computation consistency.

In contrast to the linear square model, the temperature estimation algorithm based on the quadratic model exhibits lower consistency in computing results for hypothetical materials in this work. The standard deviation for this metric is close to or exceeds 100K. This indicates that the temperature estimation algorithm based on the quadratic model cannot demonstrate high consistency in the calculations of the virtual materials used in this work. This is attributed to the emissivity characteristics of the hypothetical materials used in this study, which do not conform well to the profile of the quadratic function. Consequently, the curve fit algorithm fails to find stable global optimal points, resulting in lower consistency in the computed results.

The temperature estimation algorithm based on the exponential model demonstrates comparable accuracy and consistency to the temperature estimation algorithm based on the linear square model when applied to blackbody material and materials based on model 1, 2, 3, 4, and 6. Furthermore, it offers significant time savings in computational efforts. In situations where the emissivity variation is limited, this model exhibits a higher propensity to yield stable local optima, making it particularly suitable for application in the liquid phase region of hypothetical materials based on models.

It is evident from the results that different temperature estimation algorithms exhibit varying performance when applied to experimental data from different materials. To address this, the author proposes utilizing a temperature estimation algorithm based on the mixed model to effectively combine the advantages of different estimation approaches, especially for materials with complex emissivity characteristics. Table 1 illustrates that the mixed model outperforms the linear square model and exponential model in the computation of blackbody materials, showing better accuracy and consistency. Moreover,

Table 1: Calculation results from different models

	Black body	Real data	Model 1	Model 2	Model 3	Model 4	Model 5	Model 6	Model 7	Model 8	Model 9
Linear											
Difference [K]	20.7	-151.7	129.5	38.8	58.6	116.5	-4.8	-39.6	-161.6	445.5	27.2
Rel. difference	0.02	0.08	0.08	0.03	0.04	0.08	0.02	0.04	0.11	0.32	0.02
SD [K]	7.06	9.56	115.31	44.97	73.78	98.33	57.27	104.74	112.38	157.94	20.80
Max. difference [K]	0.029	0.096	0.160	0.073	0.145	0.140	0.167	0.170	0.263	0.489	0.057
Min. difference [K]	0.006	0.076	0.0001	0.0004	0.0001	0.0001	0.00	0.0001	0.001	0.031	0.0003
Linear square											
Difference [K]	38.7	30.8	102.9	-13.1	24.4	72.9	-31.1	96.5	-122.5	423.9	-10.6
Rel. difference	0.03	0.02	0.07	0.03	0.03	0.05	0.02	0.07	0.08	0.30	0.03
SD [K]	23.95	6.88	8.21	42.45	36.18	11.12	57.39	27.09	45.99	93.41	58.86
Max. difference [K]	0.074	0.079	0.105	0.059	0.071	0.088	0.101	0.115	0.118	0.379	0.093
Min. difference [K]	0.006	0.013	0.03	0.000	0.0001	0.031	0.0001	0.011	0.018	0.03	0.0001
Quadratic											
Difference [K]	19.3	-151.7	104.7	41.5	8.6	88.1	76.7	-47.8	-212.7	509.9	113.1
Rel. difference	0.01	0.09	0.09	0.09	0.04	0.10	0.11	0.03	0.14	0.37	0.12
SD [K]	4.07	9.56	194.96	214.93	144.50	216.52	239.63	96.18	117.62	167.72	234.07
Max. difference [K]	0.022	0.096	0.336	0.329	0.280	0.352	0.321	0.166	0.280	0.630	0.341
Min. difference [K]	0.006	0.076	0.005	0.003	0.000	0.005	0.0003	0.0001	0.092	0.031	0.003
Exponential											
Difference [K]	20.5	-147.3	102.9	-12.9	24.4	72.9	-60.5	96.6	-406.4	318.2	-91.6
Rel. difference	0.01	0.08	0.07	0.03	0.03	0.05	0.04	0.07	0.45	0.325	0.235
SD [K]	16.70	24.63	8.23	42.15	36.19	11.14	56.69	27.04	523.51	385.45	343.71
Max. difference [K]	0.075	0.096	0.105	0.056	0.071	0.088	0.101	0.115	0.644	0.630	0.452
Min. difference [K]	0.006	0.013	0.031	0.00	0.0001	0.03	0.0005	0.012	0.031	0.002	0.003
Mixed model											
Difference [K]	14.6	-34.6	102.9	-12.9	24.4	72.9	-31.1	96.6	-122.5	424.16	-10.6
Rel. difference	0.01	0.02	0.07	0.03	0.03	0.05	0.02	0.07	0.08	0.30	0.025
SD [K]	6.17	53.49	8.22	42.14	36.19	11.13	57.39	27.04	45.98	93.88	85.86
Max. difference [K]	0.017	0.096	0.105	0.056	0.071	0.088	0.101	0.115	0.118	0.382	0.093
Min. difference [K]	0.00	0.006	0.03	0.000	0.0001	0.031	0.000	0.012	0.018	0.031	0.0001

across all other models, the temperature estimation algorithm based on the mixed model consistently yields the better result in the two original temperature estimation algorithms.

5.2.2 Performance of temperature estimation algorithm between different materials

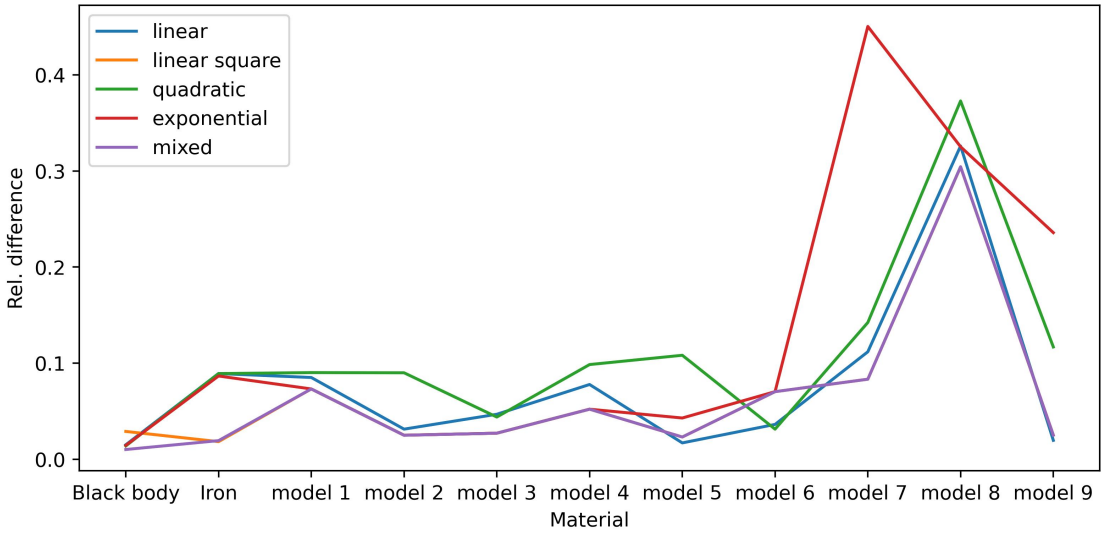

(a) Mean relative error

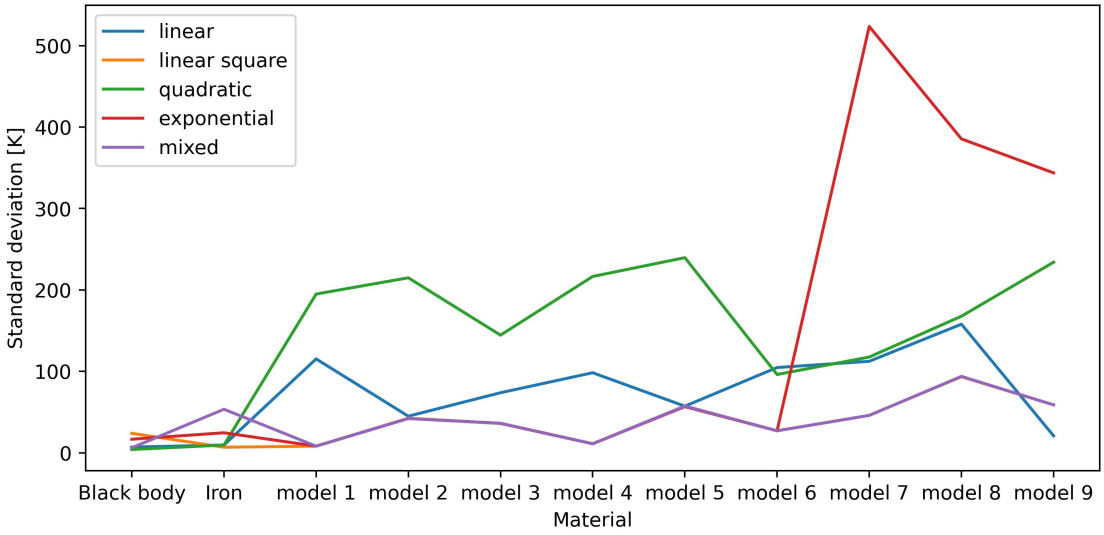

(b) Standard deviation

Figure 32: Mean relative error and standard deviation of calculation results

Fig.32 presents the computational results of temperature estimation using five different temperature estimation algorithms on various hypothetical materials.

In temperature estimation for blackbody materials, all emissivity models yield accurate results with acceptable consistency. This phenomenon arises from the fact that the emissivity of blackbody materials remains constant regardless of wavelength. This characteristic allows the avoidance of emissivity's impact on the estimated temperature during the curve fitting process, thus enhancing both the accuracy and consistency of the calculations.

In the calculation of hypothetical material based on real iron data, the temperature

estimation algorithms based on the linear square model and the mixed model exhibit mean relative errors below 5%. Other models also achieve mean relative errors below 10%. Concerning computational consistency, apart from the mixed model and exponential model, the standard deviations of the remaining models are within 10K, while the mixed model and exponential model have standard deviations exceeding 20K. This phenomenon is attributed to the exponential model's inability to adequately fit the emissivity behavior within the liquid phase region of real iron data. Consequently, this inadequacy leads to a decrease in the accuracy of temperature estimation. Meanwhile, it is noteworthy that the temperature estimation algorithm based on the mixed model alters the emissivity model during its operation, thereby resulting in a reduction in the consistency of the computed results.

In contrast to the first two materials, for materials based on model 1, 2, 3, 4, 5, 6, and 9, the mixed model and linear square model exhibit similar performance in temperature estimations. Both models are capable of achieving a mean relative error in temperature estimation of less than 10%. On the other hand, the quadratic model demonstrates relatively inferior performance. Its computational result exhibit both higher mean relative error and lower consistency in calculations. This observation suggests that the temperature estimation algorithm based on the quadratic model is not suitable for calculating temperatures of the hypothetical materials mentioned in this work. Conversely, the temperature estimation algorithms based on the linear square model and the mixed model can achieve higher precision in temperature estimation for these hypothetical materials.

For models 7 and 8, all temperature estimation algorithms exhibit lower computational accuracy and consistency. Particularly in model 8, none of the five temperature estimation algorithms are capable of providing effective temperature estimation results. This issue arises from the inability of these algorithms to fit the emissivity behavior of model 8, leading to ineffective temperature estimation results. Consequently, it is evident that the emissivity model plays a crucial role in temperature estimation algorithms, serving as a key determinant of their accuracy and consistency.

5.3 System limitations and boundaries

In the aforementioned analysis, it can be observed that the virtual experimentation platform, along with the temperature estimation system, are not devoid of imperfections. During utilization, they also exhibit certain limitations and systemic boundaries.

5.3.1 Raw material data in virtual experiment platform

5.3.2 Temperature estimation algorithm at high target temperature

5.3.3 Emissivity model in temperature estimation algorithm

6 Conclusion and prospects

Bibliography

[1] Frazier, W. E., "Metal additive manufacturing: A review", *Journal of Materials Engineering and Performance*, vol. 23, no. 6, pp. 1917–1928, 2014, ISSN: 1544-1024. DOI: 10.1007/s11665-014-0958-z. [Online]. Available: https://link.springer.com/article/10.1007/s11665-014-0958-z.

[2] Swift, K. G. and Booker, J. D., "Rapid prototyping processes", in *Manufacturing process selection handbook*, Swift, K. G. and Booker, J. D., Eds., Amsterdam: Elsevier, 2013, pp. 227–241, ISBN: 9780080993607. DOI: 10.1016/B978-0-08-099360-7.00008-2.

[3] Kruth, J. P., "Material incress manufacturing by rapid prototyping techniques", *CIRP Annals*, vol. 40, no. 2, pp. 603–614, 1991, ISSN: 0007-8506. DOI: 10.1016/S0007-8506(07)61136-6. [Online]. Available: https://www.sciencedirect.com/science/article/pii/s0007850607611366.

[4] Revilla-León, M., Meyer, M. J., and Özcan, M., "Metal additive manufacturing technologies: Literature review of current status and prosthodontic applications", *International Journal of Computerized Dentistry*, pp. 55–67, 2019.

[5] Oliveíra, J., LaLonde, A., and Ma, J., "Processing parameters in laser powder bed fusion metal additive manufacturing", *Materials & Design*, vol. 193, p. 108 762, 2020, ISSN: 0264-1275. DOI: 10.1016/j.matdes.2020.108762. [Online]. Available: https://www.sciencedirect.com/science/article/pii/s0264127520302963.

[6] DebRoy, T., Wei, H. L., Zuback, J. S., Mukherjee, T., Elmer, J. W., Milewski, J. O., Beese, A. M., Wilson-Heid, A., De, A., and Zhang, W., "Additive manufacturing of metallic components – process, structure and properties", *Progress in Materials Science*, vol. 92, no. 5, pp. 112–224, 2018, ISSN: 00796425. DOI: 10.1016/j.pmatsci.2017.10.001.

[7] Li, D., Liu, R., and Zhao, X., *Overview of in-situ temperature measurement for metallic additive manufacturing: How and then what*, 2019. DOI: 10.26153/TSW/17384.

[8] Hagqvist, P., Sikström, F., and Christiansson, A.-K., "Emissivity estimation for high temperature radiation pyrometry on ti–6al–4v", *Measurement*, vol. 46, no. 2, pp. 871–880, 2013, ISSN: 02632241. DOI: 10.1016/j.measurement.2012.10.019.

[9] Pixner, F., Buzolin, R., Schönfelder, S., Theuermann, D., Warchomicka, F., and Enzinger, N., "Contactless temperature measurement in wire-based electron beam additive manufacturing ti-6al-4v", *Welding in the World*, vol. 65, no. 7, pp. 1307–1322, 2021, ISSN: 1878-6669. DOI: 10.1007/s40194-021-01097-0. [Online]. Available: https://link.springer.com/article/10.1007/s40194-021-01097-0.

[10] J. Scott, N. Gupta, C. Wember, S. Newsom, and T. Caffrey, *Additive Manufacturing: Status and Opportunities*. 2012. [Online]. Available: https://www.researchgate.net/profile/justin-scott-4/publication/312153354_additive_manufacturing_status_and_opportunities.

[11] Hartke, K., *Manufacturing Technology Support (MATES). Task Order 0021: Air Force Technology and Industrial Base Research and Analysis, Subtask Order 06: Direct Digital ….* 2011. [Online]. Available: https://apps.dtic.mil/sti/citations/tr/ada551779.

[12] Mazzoli, A., "Selective laser sintering in biomedical engineering", *Medical & Biological Engineering & Computing*, vol. 51, no. 3, pp. 245–256, 2013, ISSN: 1741-0444. DOI: 10.1007/s11517-012-1001-x. [Online]. Available: https://link.springer.com/article/10.1007/s11517-012-1001-x.

[13] Wong, K. V. and Hernandez, A., "A review of additive manufacturing", *ISRN Mechanical Engineering*, vol. 2012, pp. 1–10, 2012, ISSN: 2090-5130. DOI: 10.5402/2012/208760. [Online]. Available: http://dx.doi.org/10.5402/2012/208760.

[14] Fischer, P., Karapatis, N., Romano, V., Glardon, R., and Weber, H. P., "A model for the interaction of near-infrared laser pulses with metal powders in selective laser sintering", *Applied Physics A*, vol. 74, no. 4, pp. 467–474, 2002, ISSN: 1432-0630. DOI: 10.1007/s003390101139. [Online]. Available: https://link.springer.com/article/10.1007/s003390101139.

[15] Hooper, P. A., "Melt pool temperature and cooling rates in laser powder bed fusion", *Additive Manufacturing*, vol. 22, no. Supplement C, pp. 548–559, 2018, ISSN: 22148604. DOI: 10.1016/j.addma.2018.05.032.

[16] Osakada, K. and Shiomi, M., "Flexible manufacturing of metallic products by selective laser melting of powder", *International Journal of Machine Tools and Manufacture*, vol. 46, no. 11, pp. 1188–1193, 2006, ISSN: 0890-6955. DOI: 10.1016/j.ijmachtools.2006.01.024. [Online]. Available: https://www.sciencedirect.com/science/article/pii/s0890695506000307.

[17] Swift, K. G. and Booker, J. D., Eds., *Manufacturing process selection handbook*. Amsterdam: Elsevier, 2013, ISBN: 9780080993607.

[18] Matthews, M. J., Guss, G., Khairallah, S. A., Rubenchik, A. M., Depond, P. J., and King, W. E., Eds., *Additive manufacturing handbook: Product development for the Defense industry* (Systems innovation series). Boca Raton: CRC Press Taylor & Francis Group, 2017, ISBN: 9781315119106.

[19] Krauss, H., Eschey, C., and Zaeh, M. F., *Thermography for monitoring the selective laser melting process*, 2012. DOI: 10.26153/TSW/15406.

[20] Mani, M., Lane, B. M., Donmez, M. A., Feng, S. C., and Moylan, S. P., "A review on measurement science needs for real-time control of additive manufacturing metal powder bed fusion processes", *International Journal of Production Research*, vol. 55, no. 5, pp. 1400–1418, 2017, ISSN: 0020-7543. DOI: 10.1080/00207543.2016.1223378.

[21] Craeghs, T., Bechmann, F., Berumen, S., and Kruth, J.-P., "Feedback control of layerwise laser melting using optical sensors", *1875-3892*, vol. 5, pp. 505–514, 2010, ISSN: 1875-3892. DOI: 10.1016/j.phpro.2010.08.078. [Online]. Available: https://www.sciencedirect.com/science/article/pii/s1875389210005043.

[22] Craeghs, T., Clijsters, S., Kruth, J.-P., Bechmann, F., and Ebert, M.-C., "Detection of process failures in layerwise laser melting with optical process monitoring", *Physics Procedia*, vol. 39, pp. 753–759, 2012, ISSN: 18753892. DOI: 10.1016/j.phpro.2012.10.097.

[23] Chivel, Y. and Smurov, I., "On-line temperature monitoring in selective laser sintering/melting", *1875-3892*, vol. 5, pp. 515–521, 2010, ISSN: 1875-3892. DOI: 10.1016/j.phpro.2010.08.079. [Online]. Available: https://www.sciencedirect.com/science/article/pii/s1875389210005055.

[24] Bammer, F., Holzinger, B., Humenberger, G., Schuöcker, D., and Schumi, T., "Integration of high power lasers in bending tools", *Physics Procedia*, vol. 5, pp. 205–209, 2010, ISSN: 18753892. DOI: 10.1016/j.phpro.2010.08.045.

[25] Berumen, S., Bechmann, F., Lindner, S., Kruth, J.-P., and Craeghs, T., "Quality control of laser- and powder bed-based additive manufacturing (am) technologies", *Physics Procedia*, vol. 5, pp. 617–622, 2010, ISSN: 18753892. DOI: 10.1016/j.phpro.2010.08.089.

[26] Lott, P., Schleifenbaum, H., Meiners, W., Wissenbach, K., Hinke, C., and Bültmann, J., "Design of an optical system for the in situ process monitoring of selective laser melting (slm)", *Physics Procedia*, vol. 12, pp. 683–690, 2011, ISSN: 18753892. DOI: 10.1016/j.phpro.2011.03.085.

[27] Yadroitsev, I., Krakhmalev, P., and Yadroitsava, I., "Selective laser melting of ti6al4v alloy for biomedical applications: Temperature monitoring and microstructural evolution", *Journal of Alloys and Compounds*, vol. 583, pp. 404–409, 2014, ISSN: 09258388. DOI: 10.1016/j.jallcom.2013.08.183.

[28] Dinwiddie, R. B., Kunc, V., Lindal, J. M., Post, B., Smith, R. J., Love, L., and Duty, C. E., "Infrared imaging of the polymer 3d-printing process", in *Thermosense: Thermal Infrared Applications XXXVI*, Colbert, F. P. and Hsieh, S.-J., Eds., ser. SPIE Proceedings, SPIE, 2014, p. 910 502. DOI: 10.1117/12.2053425.

[29] Price, S., Cooper, K., and Chou, K., *Evaluations of temperature measurements by near-infrared thermography in powder-based electron-beam additive manufacturing*, 2012. DOI: 10.26153/TSW/15387.

[30] Price, S., Lydon, J., Cooper, K., and Chou, K., *Experimental temperature analysis of powder-based electron beam additive manufacturing*, 2013. DOI: 10.26153/TSW/15422.

[31] Rodriguez, E., Medina, F., Espalin, D., Terrazas, C., Muse, D., Henry, C., MacDonald, E., and Wicker, R. B., *Integration of a thermal imaging feedback control system in electron beam melting*, 2012. DOI: 10.26153/TSW/15402.

[32] Wegner, A. and Witt, G., *Process Monitoring in Laser Sintering Using Thermal Imaging*. University of Texas at Austin, 2011. DOI: 10.26153/tsw/15303. [Online]. Available: https://repositories.lib.utexas.edu/handle/2152/88364.

[33] Ueda, T., Hosokawa, A., and Yamamoto, A., "Measurement of grinding temperature using infrared radiation pyrometer with optical fiber", *Journal of Engineering for Industry*, vol. 108, no. 4, pp. 247–251, 1986, ISSN: 0022-0817. DOI: 10.1115/1.3187074.

[34] Raplee, J., Plotkowski, A., Kirka, M. M., Dinwiddie, R., Okello, A., Dehoff, R. R., and Babu, S. S., "Thermographic microstructure monitoring in electron beam additive manufacturing", *Scientific Reports*, vol. 7, no. 1, pp. 1–16, 2017, ISSN: 2045-2322. DOI: 10.1038/srep43554. [Online]. Available: https://www.nature.com/articles/srep43554.

[35] Doubenskaia, M., Pavlov, M., Grigoriev, S., and Smurov, I., "Definition of brightness temperature and restoration of true temperature in laser cladding using infrared camera", *Surface and Coatings Technology*, vol. 220, pp. 244–247, 2013, ISSN: 0257-8972. DOI: 10.1016/j.surfcoat.2012.10.044. [Online]. Available: https://www.sciencedirect.com/science/article/pii/s0257897212010146.

[36] Smurov, I., Doubenskaia, M., and Zaitsev, A., "Comprehensive analysis of laser cladding by means of optical diagnostics and numerical simulation", *Surface and Coatings Technology*, vol. 220, pp. 112–121, 2013, ISSN: 0257-8972. DOI: 10.1016/j.surfcoat.2012.10.053. [Online]. Available: https://www.sciencedirect.com/science/article/pii/s0257897212010237.

[37] Muller, M., Fabbro, R., El-Rabii, H., and Hirano, K., "Temperature measurement of laser heated metals in highly oxidizing environment using 2d single-band and spectral pyrometry", *Journal of Laser Applications*, vol. 24, no. 2, 2012, ISSN: 1042-346X. DOI: 10.2351/1.3701400.

[38] Grujić, K., "A review of thermal spectral imaging methods for monitoring high-temperature molten material streams", *Sensors (Basel, Switzerland)*, vol. 23, no. 3, 2023. DOI: 10.3390/s23031130.

[39] Devesse, W., Baere, D. de, and Guillaume, P., "High resolution temperature measurement of liquid stainless steel using hyperspectral imaging", *Sensors (Basel, Switzerland)*, vol. 17, no. 1, 2017. DOI: 10.3390/s17010091.

[40] Spiering, B. A. and Beach, L., "Multi spectral imaging system", pat. 5 900 942, 1999.

[41] Hagen, N. and Kudenov, M. W., "Review of snapshot spectral imaging technologies", *Optical Engineering*, vol. 52, no. 9, p. 090 901, 2013, ISSN: 0091-3286. DOI: 10.1117/1.OE.52.9.090901.

[42] BAYER B., "Color imaging array", pat. 3 971 065, 1976. [Online]. Available: https://cir.nii.ac.jp/crid/1572261550680217344.

[43] Jones, J. M., Mason, P. E., and Williams, A., "A compilation of data on the radiant emissivity of some materials at high temperatures", *Journal of the Energy Institute*, vol. 92, no. 3, pp. 523–534, 2019, ISSN: 17439671. DOI: 10.1016/j.joei.2018.04.006.

[44] Zhu, W., Shi, D., Zhu, Z., and Sun, J., "Spectral emissivity model of steel 309s during the growth of oxide layer at 800–1100 k", *International Journal of Heat and Mass Transfer*, vol. 109, pp. 853–861, 2017, ISSN: 00179310. DOI: 10.1016/j.ijheatmasstransfer.2017.02.062.

[45] Kobatake, H., Khosroabadi, H., and Fukuyama, H., "Normal spectral emissivity measurement of liquid iron and nickel using electromagnetic levitation in direct current magnetic field", *Metallurgical and Materials Transactions A*, vol. 43, no. 7, pp. 2466–2472, 2012, ISSN: 1073-5623. DOI: 10.1007/s11661-012-1101-0.

[46] Watanabe, H., Susa, M., Fukuyama, H., and Nagata, K., "Phase (liquid/solid) dependence of the normal spectral emissivity for iron, cobalt, and nickel at melting points", *International Journal of Thermophysics*, vol. 24, no. 2, pp. 473–488, 2003, ISSN: 1572-9567. DOI: 10.1023/A:1022924105951. [Online]. Available: https://link.springer.com/article/10.1023/a:1022924105951.

[47] Krishnan, S., Yugawa, K. J., and Nordine, P. C., "Optical properties of liquid nickel and iron", *Physical Review B*, vol. 55, no. 13, pp. 8201–8206, 1997, ISSN: 0163-1829. DOI: 10.1103/PhysRevB.55.8201.

[48] Taunay, P.-Y. C. R. and Choueiri, E. Y., "Multi-wavelength pyrometry based on robust statistics and cross-validation of emissivity model", *The Review of scientific instruments*, vol. 91, no. 11, p. 114 902, 2020. DOI: 10.1063/5.0019847.

[49] Wang, N., Shen, H., and Zhu, R., "Constraint optimization algorithm for spectral emissivity calculation in multispectral thermometry", *Measurement*, vol. 170, p. 108 725, 2021, ISSN: 02632241. DOI: 10.1016/j.measurement.2020.108725.

[50] Kuhn, T. S., *Black-Body Theory and the Quantum Discontinuity, 1894-1912*. University of Chicago Press, 1987, ISBN: 9780226458007.

[51] Fossum, E. R. and Hondongwa, D. B., "A review of the pinned photodiode for ccd and cmos image sensors", *IEEE Journal of the Electron Devices Society*, vol. 2, no. 3, pp. 33–43, 2014. DOI: 10.1109/JEDS.2014.2306412.

[52] Asanovic, K., Bodik, R., Demmel, J., Keaveny, T., Keutzer, K., Kubiatowicz, J., Morgan, N., Patterson, D., Sen, K., Wawrzynek, J., Wessel, D., and Yelick, K., "A view of the parallel computing landscape", *Communications of the ACM*, vol. 52, no. 10, pp. 56–67, 2009, ISSN: 0001-0782. DOI: 10.1145/1562764.1562783.

List of Abbreviations

AM	Additive Manufacturing
BJT	Binder Jetting
CCD	Charge-coupled device
CMOS	Complementary Metal-oxide Semiconductor
DED	Direct Energy Deposition
LBAM	Professorship Laser-based Additive Manufacturing
MEX	Material Extrusion
MJT	Material Jetting
MSI	Multispectral Imaging
PBF	Powder Bed Fusion
PBF-LB	Laser-based Powder Bed Fusion
PBF-LB/M	Laser-based Powder Bed Fusion of Metals
SHL	Sheet Lamination
SLM	Selective Laser Melting
SLS	Selective Laser Sintering
VPP	Vat Photopolymerization

Disclaimer

I hereby declare that this thesis is entirely the result of my own work except where otherwise indicated. I have only used the resources given in the list of references.

Garching, August 29, 2023

(Signature)